2013

Desktop microforming and welding system powered by a flextensional Terfenol-D transducer

Adam Timothy Witthauer
Iowa State University

Desktop microforming and welding system powered by a flextensional Terfenol-D transducer

by

Adam Witthauer

A dissertation submitted to the graduate faculty

in partial fulfillment of the requirements for the degree of

DOCTOR OF PHILOSOPHY

Major: Mechanical Engineering

Program of Study Committee:
Gap-Yong Kim, Major Professor
LeAnn Faidley
Qingze Zou
Alan Russell
Lester Schmerr

Iowa State University

Ames, Iowa

2013

DEDICATION

This dissertation is dedicated to my parents,

Mr. and Mrs. Tim and Marla Witthauer and Mrs. Peggy Witthauer

for their love and invaluable support.

TABLE OF CONTENTS

LIST OF FIGURES

LIST OF TABLES

ACKNOWLEDGEMENTS

I would like to take this opportunity to express my deepest appreciation to my advisors present and past, Prof. Gap-Yong Kim and Prof. LeAnn Faidley, for their great support, guidance and patience throughout my Ph.D. study and research. I would also like to extend my appreciation to Prof. Zou, Prof. Russell and Prof. Schmerr for their invaluable lecture teaching and guidance.

ABSTRACT

Magnetostrictive Terfenol-D was examined as a prime-mover for bulk motion in a microforming system. Careful design and analysis led to the creation of a Terfenol-D transducer capable of 3.8 kN of blocked force and 212 μm of displacement. A linear model of the Terfenol-D transducer to simulate its output as a function of displacement under saturation magnetic field was created that matched both force and displacement within 10%. Thermal drift occurred at a rate of 2 μm/ºC. A flextensional lever system was designed to amplify the displacement of the Terfenol-D transducer to levels sufficient for microforming. Sub-micron displacement resolution was observed, with no perceivable effects from friction or backlash. The full system provided 365 N of blocked force and 1.6 mm of displacement. A linear model of the full system was also created that used the linear model of the transducer's output which matched experimental results for displacement with a 2% error and force with an 11% error, which was found to be useful for selection of design parameters.

In ultrasonic-assisted punching, a circular punch of 3.2 mm diameter that vibrates transversely at 9.6 kHz was used to punch samples of 1100-O at several punching speeds and vibration intensities. Higher speed punching tests showed up to a 30% reduction in punching force accompanied by an apparent elimination of adiabatic strain rate effects. Lower speed punching showed a smaller degree of softening, but an increased burnished-to-fractured area ratio.

A study on the effects of vibration waveform on a polymer vibration welding process on 0.25 and 0.5 mm ABS sheet was conducted using sine, square, and triangle waves at differing penetration depths. A preliminary study was first used to determine control levels of basic welding parameters that compared the effects of clamping load and penetration depth on the two sheet thicknesses. It was found that square waves provided slightly higher penetration rates than sine waves, and triangle waves significantly lower penetration rates than sine waves. Penetration rates and achievable penetration depths varied with sheet thickness. A minimum penetration rate threshold was found below which it was not possible to achieve adequate penetration; beyond this lower penetration rates generally resulted in higher strength.

CHAPTER 1. INTRODUCTION

1.1 Motivation

Micromanufacturing is a growing field spurred by the drive for miniaturization, with many new applications in MEMs, electronics, and medical devices to name a few. Several challenges are unique to microforming compared to conventional forming processes. Geometric scaling becomes an issue as the achievable tolerance on conventional forming processes becomes a relatively large proportion of the part dimensions for a micro-part. Material property assumptions that hold well on the scale of millimeters or more lose validity when geometric features approach grain diameter dimensions. Increased precision requirements drive up tooling costs as well. Another motivation in developing microforming systems is the reduction in size of the equipment used. With shop space always at a premium, it is quite desirable to have table top systems that not only take up less space but are also much simpler and cheaper to transport and set up.

Much research has already been accomplished in micro-machining, including many models and machines created for micro-turning and micro-milling. The market for micro machine tools has reached the level of maturity that high-precision desktop machines are available from major machine tool manufacturers, such as the micro-machining center shown in Figure 1 that uses zero backlash technology and thermal control to achieve nano-scale surface finish (MoriSeiki, 2012).

Figure 1 Micro-machining center by Mori Seiki that provides nano-scale surface finish through zero backlash technology and thermal control (MoriSeiki, 2012).

Microforming processes have seen much less development. Some conventional processes such as drawing regularly result in part geometry with dimensions in the micro-scale, but other processes such as micro-extrusion and micro-punching show challenges in the micro-scale that are yet to be overcome. Machines used for conventional forming are also typically very large and heavy. Conventional forming offers significant cost advantages over conventional machining; these same advantages apply at the micro-scale, which emphasizes the need for microforming machines.

When creating forming machines at a new scale it is worthwhile to consider the methods used to provide forming loads. Conventional forming machines often use hydraulic power or screw drive. Hydraulic power is capable of providing very large loads, although at the expense of providing and maintaining not only actuators, but oil reservoirs and high-pressure plumps, plumbing, and controls. Hydraulic components are typically not available in a size suitable for a desktop machine, as there is not a large demand for the brute force and

complexity to justify a hydraulic system for machines small enough to fit on a desktop. The price and complexity are simply not justifiable. Screw drive systems can scale down to the desktop size nicely; however the effects of backlash in a screw drive system are magnified when scaling to the micro-scale.

The simplicity offered by electrostrictive or magnetostrictive materials is quite attractive for a desktop-sized solution. Terfenol-D was examined for use in this application, as it has higher power density than common piezoelectric materials (Moffett, 1993), and the magnetostrictive effect of Terfenol-D is inherent to the material and does not degrade with usage (Dapino, 2004).

1.2 Research framework and objectives

The goal of this research is to develop a complete microforming system, and falls into two primary categories. The first two chapters outline the design and development of a microforming machine to provide the bulk motion for microforming. This system requires precise motion, free of friction and backlash, and moderate force levels. It uses Terfenol-D coupled with a flextensional lever system to accomplish this. The second portion of this research takes a closer look at two particular micromanufacturing processes in metal punching and plastic welding that can benefit from the size, precision and ease of control of the bulk motion machine and demonstrate its flexibility.

1.2.1 Design and characterization of a high-power, low-frequency Terfenol-D transducer for use in microforming

A high-power, low-frequency Terfenol-D transducer built around an 18 mm diameter, 200 mm long rod, was developed as a precision prime mover for a microforming application in order to examine the feasibility of using magnetostrictive materials to provide forming loads. The mechanical and magnetic design were considered, with emphasis on a simple, stiff, low-friction design with an adjustable preload system capable of supporting up to a 20 MPa preload with a spring rate low enough to reduce loss in output due to spring compression. A good magnetic flux return path was ensured by providing a low reactance magnetic circuit and using 416 stainless steel in key components, chosen for its combination of surface finish, strength, and ferromagnetic properties. A linear model of the system at magnetic saturation matched no-load displacement within 6% and blocked force within 8%. As tested, the system was capable of 3.8 kN blocked force and a 212 μm stroke. Simple compressed air cooling was used, which was adequate for a 10% duty cycle with temperatures stable within 1ºC. Thermal testing from 25º-45º showed thermal drift of 44 μm with a 10% loss in range. Hysteresis was present at frequencies over 5 Hz, and by 20 Hz resulted in a loss of dynamic travel of nearly 90 μm.

1.2.2 Design and characterization of a displacement amplification system for use in microforming

A lever system using flexure joints, similar to those used in flextensional actuators was designed to amplify the displacement of the Terfenol-D transducer described in detail in

Chapter 2. The system was modeled in order to compare the effects of flexure joint parameters on the system's output. Separate bolt-on flexure joints were used instead of a traditional monolithic flextensional lever system design in order to reduce cost.

1.2.3 Experiments and analysis in ultrasonic-assisted punching in aluminum

Significant research has been done to describe ultrasonic softening in terms of plasticity and stress reduction during forming, although very little is known about the effect of ultrasonic softening on fracture and fatigue, nor is current theory capable of predicting these effects. While it is known that a main component in ultrasonic softening includes an increase in dislocation mobility, it is unclear whether the increase in plasticity experienced would increase the overall ductility at extreme levels of strain, or if the accumulation of dislocations, which is visible in the form of acoustic hardening, would decrease overall ductility. Previous research also does not address the potential of increased dislocation mobility in ultrasonic softening to offset the decreased dislocation mobility that is known to cause strain rate hardening during nearly adiabatic conditions found at higher strain rates.

A micro-punching system was developed to determine this, and ultrasonic-assisted punching experiments were carried out with aluminum 1100-O. Punching was chosen as it is a process with highly localized stress concentrations that is marked by a requirement for complete material fracture. The effect of ultrasonic softening on this process can be seen not only in the force required for punching, but also in its effect on perceived strain rate effects at higher punching speeds. In this study, a circular punch of 3.2 mm diameter that vibrates

transversely at 9.6 kHz was used to punch samples of 1100-O at three vibration amplitudes and two punching speeds.

1.2.4 Effect of waveform on polymer vibration welding in ABS

Finally, minor modifications were made to the complete microforming setup to outfit it for plastic welding. The bulk motion system described in 1.2.1 and 1.2.2 was used for simple force and displacement control for an in-depth study of the use of different waveforms on polymer vibration welding on ABS plastic sheet. Previous work by others has studied the effects of frequency (Stokes, 1988b) as well as simultaneously using multiple harmonics while welding (Tsujino, 2004), although none yet have investigated the effect of different waveforms. A basic Fourier analysis reveals that square waves and triangle waves can be described by a superposition of many other sine waves of varying frequency and amplitude. The frequency content for these waveforms is relatively complex compared to existing research, and takes advantage of the wider frequency response exhibited by the Terfenol-D vibration transducer as compared to the piezoelectric transducers typically used in plastic welding.

A study on the effects of vibration waveform on a polymer vibration welding process on 0.25 and 0.5 mm ABS sheet was conducted using sine, square, and triangle waves. A preliminary study was first used to determine control levels of basic welding parameters that compared the effects of clamping load and penetration depth on the two sheet thicknesses. Once the process was characterized and good initial parameters were chosen the study was repeated, looking at the effects of the different waveforms with varying penetration depths.

1.3 Dissertation organization

The remainder of this report is divided into five chapters. Chapter 2 outlines the development and characterization of the high-power, low-frequency Terfenol-D transducer used to provide bulk motion to the microforming system. Transducer design is discussed, as well as a mathematical model to predict output force as a function of displacement and input voltage. Thermal response is examined, as well as its hysteresis response to varying frequencies. Chapter 3 does the same for the flexure lever system mated to this transducer. Chapter 4 examines the ultrasonic-assisted punching process on two aluminum alloys, and Chapter 5 looks at the combined micromanufacturing system as used to investigate the effects of different waveforms on polymer vibration welding in ABS sheet. Chapter 6 provides a summary of findings and scientific contribution.

CHAPTER 2. DESIGN AND CHARACTERIZATION OF A HIGH-POWER, LOW-FREQUENCY TERFENOL-D TRANSDUCER FOR USE IN MICROFORMING

2.1 Nomenclature

σ_T = stress present in Terfenol-D rod

$E(B)$ = Young's modulus of Terfenol-D rod (varies as a function of magnetic flux, B)

ε_x = mechanical strain of Terfenol-D rod

$\lambda(B)$ = magnetostrictive strain

F_T = transducer force

$k_T(V)$ = effective spring rate of transducer

$x_m(V)$ = magnetostrictive displacement

x_t = transducer displacement

2.2 Introduction

Terfenol-D is a magnetostrictive material that consists of terbium, iron, and dysprosium, and was developed in the U.S. Naval Ordnance Laboratory (Dapino, 2004). Magnetostrictive materials strain in response to a magnetic field, and see applications in micro-actuators (Olabi, 2008), acoustic and ultrasonic transducers, active tools to turn oval shapes on a common lathe (Products), active anti-vibration in civil engineering structures (Bartlett, 2001), and a sonar transducer capable of 212 dB (Moffett, 1995). Its chief competitors are piezoelectric materials (Moffett, 1995; Claeyssen, 1997), which are

electrostrictive. In comparison, piezoelectric materials are capable of less strain (approx. 0.1%), have approximately 5 times the hysteresis, and require more than 100 times the energy to reach saturation, although at half the cost to produce (Olabi, 2008). Research has shown that Terfenol-D has about four times the energy density of the common piezoelectric material PZT (Moffett, 1993). Another advantage of Terfenol-D over piezoelectric materials is that the magnetostrictive effect is inherent to its crystal structure, while under heavy use piezoelectric materials are known to lose their polarization. Its higher strength is also seen as a benefit in high-load applications.

Terfenol-D was investigated as a prime mover for a high-precision microforming platform. A common challenge when using Terfenol-D in a motion-based application is the relatively small amount of displacement that can be obtained. It is considered a giant magnetostrictive alloy, meaning it has amongst the highest strain response of any magnetostrictive materials currently available. Despite having one of the largest strain responses compared to other similar materials, its strain response is only up to 0.16% under a full saturation magnetic field (Dapino, 2004), which would necessitate an unfeasibly long rod in order to reach strokes on the order of 1 mm for a typical microforming process. However, large forces are possible due to the relatively high strength and stiffness of Terfenol-D, making a lever system to magnify displacement an attractive solution. Flextensional or cymbal lever systems are frequently used for displacement amplification with electrostrictive and magnetostrictive transducers (Meyer, 2001). This configuration was initially invented in 1936, and has been used in many variants since then (Rolt, 1990).

2.3 Background

Magnetostriction can be attributed to the oblong orbits of electrons in the outer valences of some metals. Iron and nickel show very small degrees of magnetostriction; not nearly enough to be of any practical purpose, and what little effect exists in these metals is often cancelled out on a bulk scale due to random grain orientation. This effect is much more pronounced in rare-earth metals, which are used as the basis for giant magnetostrictive materials.

The magnetostrictive effect is maximized when all dipoles are aligned, necessitating a single crystal structure with a specified alignment. The magnetostrictive effect still exists in polycrystalline Terfenol-D, however the available strain due to magnetostriction is much smaller (Claeyssen, 1997). Producing Terfenol-D rods as a single crystal is one factor in the relatively high cost of Terfenol-D; the other primary factor is the difficulty in separating terbium and dysprosium from commonly occurring mischmetal (Dapino, 2004).

When the material is subject to a magnetic field the dipoles rotate, as shown in Figure 2, causing the material to strain. This effect is referred to as Joule magnetostriction. Note that there is a limit to strain response that occurs at a given saturation field level, where all dipoles are fully rotated.

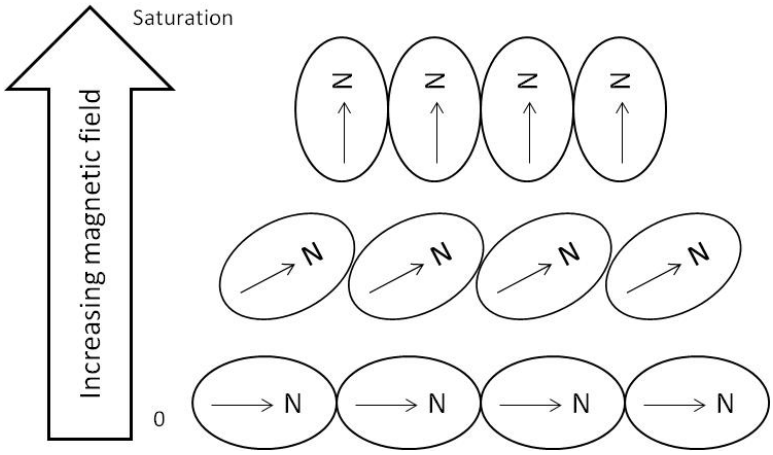

Figure 2 Magnetostriction caused by changing dipole alignment

The magnetostrictive effect causes a change in Young's Modulus that accompanies dipole rotation, known as the ΔE Effect. This effect is quite pronounced, with a seven-fold increase in stiffness from zero field to saturation (Dapino, 2004), making this a very important consideration in an application where large force is desired. Magnetic hysteresis is present, which results in a small loss as the field changes directions. Mechanical preload to the Terfenol-D rod is also required in order to get maximum strain output by ensuring all dipoles are rotated to their zero-field state (Dapino, 2004). The strain output of Terfenol-D in response to a magnetic field is generally non-linear, and varies with the amount of preload present. A typical preload for a Terfenol-D transducer is about 20 MPa.

The displacement output is generated by strain, therefore the output is elastic (although not linear), acting similar to a spring from a design standpoint. Maximum force occurs at zero displacement; this is typically referred to as blocked force (Olabi, 2008). Several other magnetostrictive effects occur which are listed in Table 1. Note that for every effect its inverse holds true. For example, the Villari effect can be used to create sensors

such as load cells or accelerometers, much in the same way piezoelectric materials are used in these applications.

Table 1 Magnetostrictive effects (Dapino, 2004)

Direct Effects	Inverse Effects
Joule magnetostriction Change in sample dimensions in the direction of the applied field	**Villari effect** Change in magnetization due to applied stress
ΔE effect Magnetoelastic contribution to magnetocrystalline anisotropy	Magnetically induced changes in elasticity
Wiedemann effect Torque induced by helical anisotropy	**Matteuci effect** Helical anisotropy and e.m.f. induced by a torque
Magnetovolume effect Volume change due to magnetostriction (most evident near the Curie temperature)	**Nagaoka-Honda effect** Change in the magnetic state due to a change in the volume

Magnetic bias is another typical design consideration for magnetostrictive actuators. When an electric coil is the only source of magnetic field, a positive voltage input may cause the strain response as shown in Figure 2 where the dipoles rotate to the left, while a negative voltage will cause the dipoles to rotate to the right; the strain response for both conditions is in the same direction. Therefore, a transducer without a permanent magnet bias that is subject to a sine wave input will respond at twice the input frequency (Dapino, 2004).

Several novel magnetostrictive actuator configurations have been developed in previous research. One notable model that effectively increases the displacement output considerably is the Kiesewetter motor (Claeyssen, 1997). The operation of this motor, whose operation is similar to that of a walking inchworm, is shown in detail in Figure 3. This motor takes advantage of the Poisson effect and force is provided by friction. A magnetostrictive

rod sits within a tube with a tight interference fit. This interference fit defines the holding power of the motor. A small coil provides a magnetic field over a very small portion of the length of the rod, causing localized magnetostriction, which not only results in a longitudinal strain of the rod, but also a radial shrinking which relaxes the interference fit in that portion of the rod. Moving the coil down the rod causes the "inchworm style" motion, which is finally realized when the coil reaches the end of the rod. Using a 10 mm diameter, 120 mm long rod, speeds of up to 20 mm/s, 1000 N of force, and resolution of 2 μm are possible (Claeyssen, 1997). The disadvantages to this style of motor are inefficiency and wear (Claeyssen, 1997).

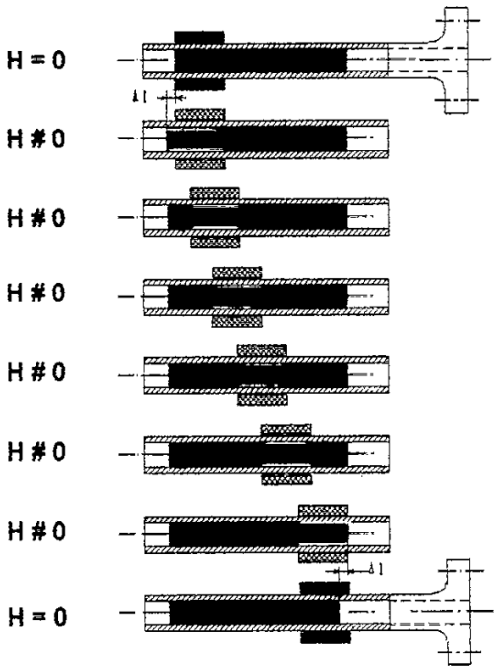

Figure 3 Kiesewetter motor principle (Claeyssen, 1997)

Sputtering has been used to apply thin films of Terfenol-D to materials to create micro-actuators. Due to the fact that single crystal materials cannot be created through

sputtering, strain output is lower, but the operation of these micro-motors is fascinating nonetheless. An example of a linear micro-motor is shown in Figure 4. Tiny feet are attached to a silicon plate with alternating strips of Terfenol-D applied by sputtering. An AC magnetic field is applied from above the plate at its natural frequency, which causes the feet to oscillate, inducing motion with velocity on the order of mm/s.

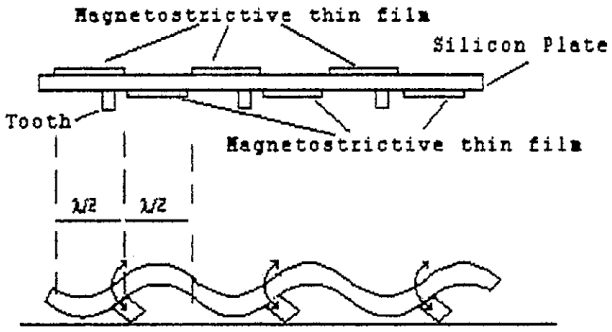

Figure 4 Wireless linear micro motor (Claeyssen, 1997)

2.4 Transducer design and modeling

Given that Terfenol-D is capable of approximately 0.12% strain in a static configuration (Dapino, 2004) and are available from Etrema Products in lengths of up to 200 mm, a lever ratio of 10 was chosen to meet displacement requirements, and a rod diameter of 18 mm was chosen to meet force requirements with this lever ratio. No commercially available Terfenol-D actuators exist that fulfill the requirements of this design, so one was designed and fabricated for this purpose. No bias magnets were included as frequency doubling is not a concern, but compact packaging was a criterion. Another advantage from a control aspect is that the minimum stroke occurs at zero voltage, allowing a failsafe that under loss of power the actuator will return to minimum stroke.

An additional design constraint for magnetostrictive transducers is ensuring an efficient magnetic return path for the flux. Decreasing the magnetic reactance results in greater magnetic response per voltage input, which increases system output per voltage input. An axisymmetric magnetic finite element method (FEM) was built in COMSOL to model the magnetic response of the actuator. The results are shown in Figure 5. The flux source is given as the Terfenol-D rod (center-most rectangle in the figure), using a field strength of 100 kA/m^2. The outer casing is made of plain carbon steel, which offers a simple solution for the outer casing as well as an effective magnetic flux return path. The end caps and slider are made of 416 stainless steel, which was chosen for its ferromagnetic properties. The right-hand cap is the fixed-end of the transducer, and includes a bolt for adjusting preload against the belleville spring stack, which appear as parallelograms on the left-hand side, and rest against the output slider (also 416 stainless steel).

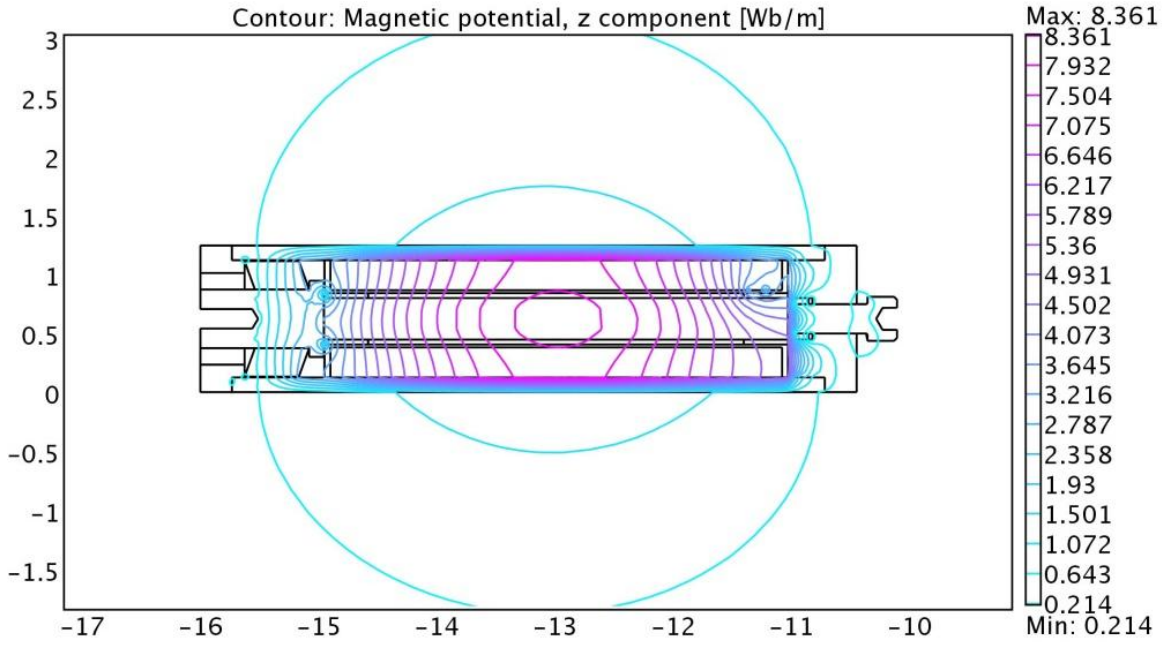

Figure 5 Magnetic FEM results

Each of the colored lines in Figure 5 represents a magnetic potential. The proximity of these lines to each other is an indication of the flux density. From this figure it is clear that the outer casing and fixed end cap on the right hand side of the figure provide effective flux return paths, however on the left-hand side of the casing the less-dense flux line spacing through the belleville spring stack indicates a relatively inefficient flux return path.

For the final model, two stacks of belleville springs in series-parallel were chosen to not only improve the flux return path, but also support up to a 20 MPa preload while providing a low enough spring rate to prevent from providing unnecessarily high force at maximum displacement which would compromise displacement output. The output slider diameter was also increased to improve the flux return path. Figure 6 shows a fully detailed cutaway of the transducer as produced.

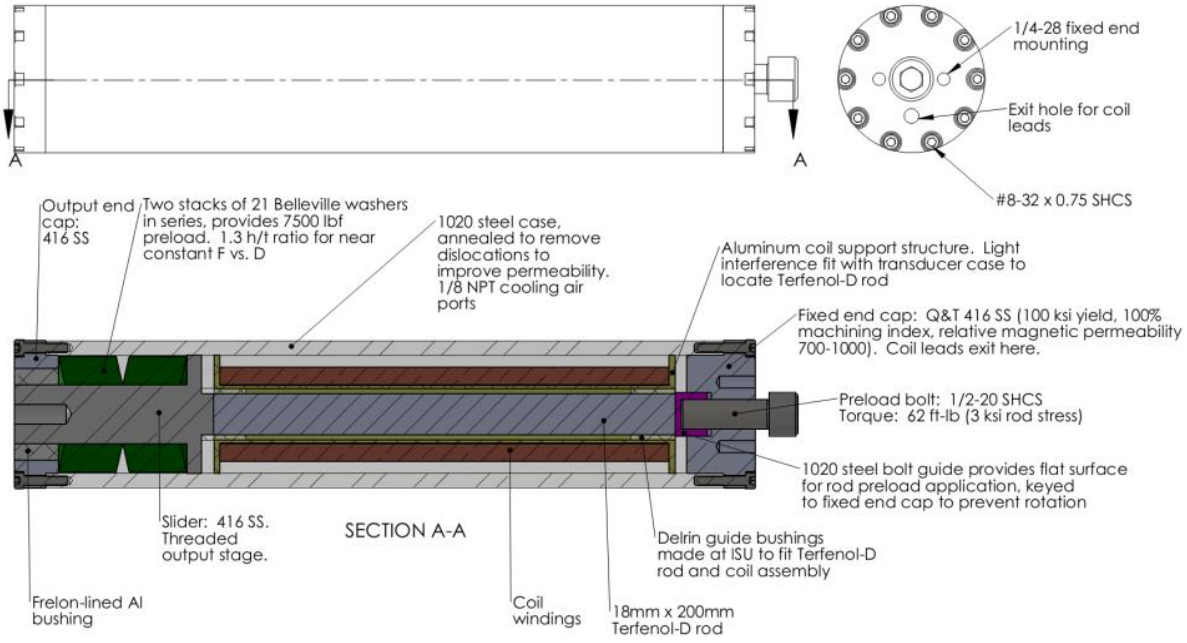

Figure 6 Schematic of Terfenol-D actuator

From a mechanical design aspect, an important factor is designing the system for purely axial loading on the Terfenol-D rod. Terfenol-D is relatively brittle and while its compressive strength is relatively high, its tensile strength is not. Therefore from a purely structural standpoint bending and torsional loads should be avoided. From a performance standpoint it is also very important to avoid bending loads, as angular deflection in the rod and slider can cause binding and friction, which cause stiction every time direction changes, which ruins repeatability and drastically increases the "minimum step" resolution the system can make. On this transducer, torsional and bending loads were eliminated through several strategies: 1) On the fixed end which housed the adjusting bolt, the bolt face did not act directly on the Terfenol-D rod, but instead on a cup with a machined contact face that rode in a guide that was keyed to the housing to prevent rotation. 2) The rod itself rode on Delrin

bushings within the coil that were machined with a loose interference fit tolerance, which by Poisson's law became a looser fit as the rod expanded. 3) On the output side, the system output slider rode within a Frelon-lined plain bearing. The bearing retainer was also machined with a loose interference fit, such that it would not fall out due to gravity, but 5 psi of compressed air would blow it out (before proper staking of the bearing was applied). Bending loads on the slider were eliminated by choosing axisymmetric Belleville springs over more conventional coil springs which apply a non-axisymmetric bending load where the end of the coil rests, even with closed and ground ends. To minimize tolerance stackup both end caps and the Al coil bobbin were machined to a light press fit (some resistance when assembling by hand) with the tubular transducer housing.

To a first approximation under static conditions, the operation of the Terfenol-D rod is of a linearly elastic material whose strain state and Young's Modulus varies as a function of magnetic field (Moffett, 1991). Therefore its static response can be simply modeled as a linear spring using a modified form of Hooke's Law,

$$\sigma_T = E(B)\left(\varepsilon_x - \lambda(B)\right) \tag{1}$$

where σ_T is the stress in the Terfenol-D rod, and Young's Modulus E and magnetostrictive strain λ are functions of magnetic field strength B (Dapino, 2004). ε_x is the axial strain of the material due to externally applied stresses, which describes the actual displacement output of the rod allowed by boundary conditions. Conceptually speaking, there are two primary boundary conditions used to evaluate the linear spring behavior of the Terfenol-D rod. The

first is the case of free displacement where the rod is allowed to strain freely due to magnetostriction, where $\varepsilon_x = \lambda$. In this case, because the output strain is the same as the magnetostrictive strain, the stress is zero. The opposite condition is the blocked force condition, where the output displacement is blocked and $\varepsilon_x = 0$. In this case the free length without load is λ, ε_x is held at zero, and stress is maximum. This condition is conceptually similar to a rod whose displacement is fixed, is heated, and experiences stress due to thermal expansion.

Because E and λ are nonlinear functions of field strength, and because field strength is a function of system voltage, the simplest method of obtaining strain response due to magnetostriction is to simply measure the no-load displacement response of the transducer as a function of voltage, $x_m(V)$. Using Hooke's Law relationships, it is possible to convert stress to a force, Young's Modulus to an equivalent spring rate, and strain to a displacement. Comparing the actual displacement of the transducer, x_T with $x_m(V)$ and the effective spring rate of the transducer $k_T(V)$ gives the force response of the transducer, $F_T(V)$.

$$F_T(V) = k_T(V)\left(x_m(V) - x_T\right) \tag{2}$$

2.5 Experimental setup

A computer-controlled data acquisition and control system was used to generate inputs to the system and measure its response. The bulk motion transducer and its mounting within the test rig for force and displacement testing is shown in Figure 7.

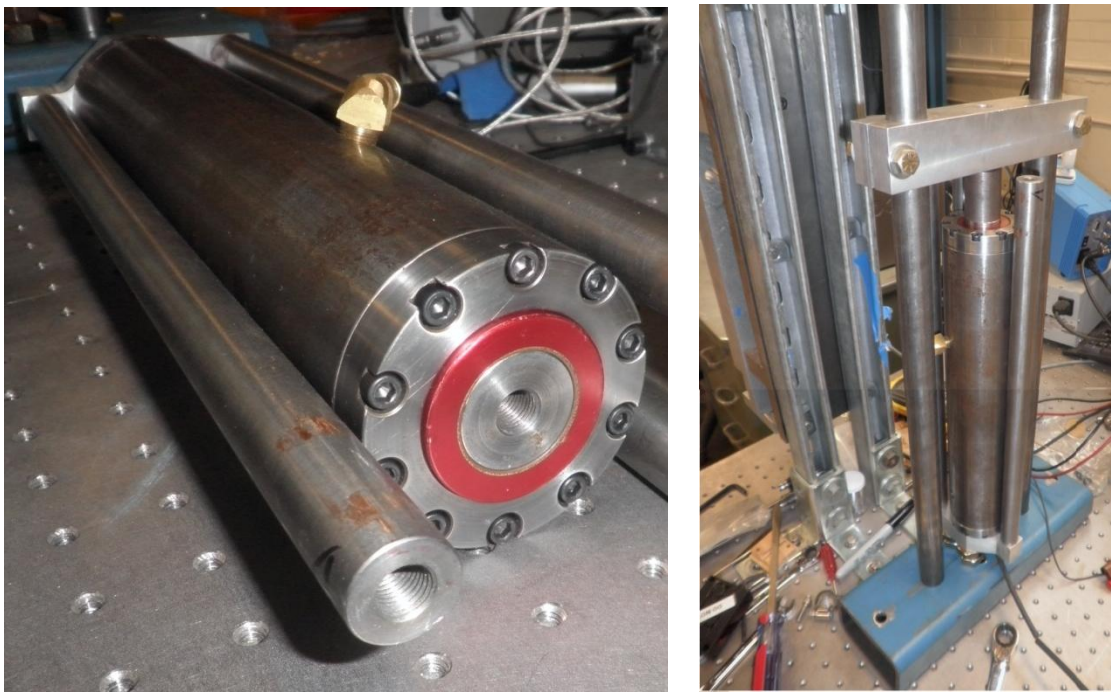

Figure 7 Terfenol-D bulk motion transducer

The data acquisition and control system is outlined in Figure 8, and is built around a Matlab Simulink model to handle inputs and outputs. This model is interfaced with measurement and control hardware via an XPC Target PC that houses analog input and output cards. A sample frequency of 1 kHz was used throughout. The only system output is for the coil voltage for the Terfenol-D transducer, which is fed to a Techron 7700 series 3-phase amplifier capable of +/- 200V. Measurements taken include force at the output stage of the transducer and two non-contact displacement sensors, which consist of a laser displacement sensor with a 5 mm range for coarse, large-displacement measurements, and a capacitive displacement sensor with a 750 μm range for high-resolution measurements. All measurement channels were connected with differential inputs.

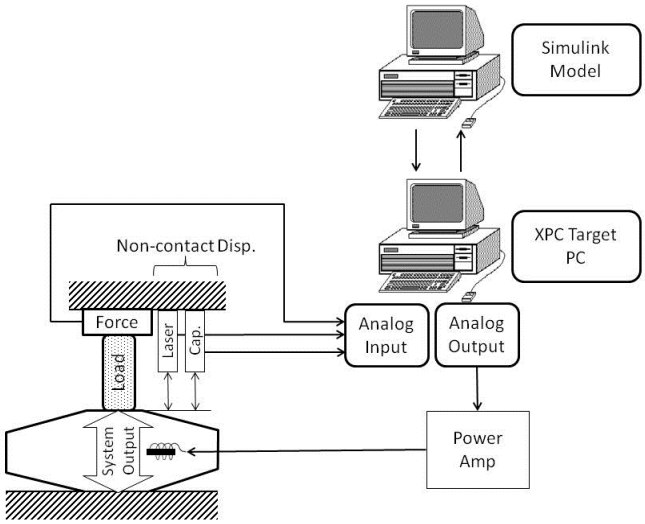

Figure 8 Measurement and control system setup

2.6 Results and discussion

The first test taken was to find the preload in the Terfenol-D rod that yielded the largest displacement. Tests were conducted up to 20 MPa, and a preload of 3.4 MPa was found to give the largest displacement and blocked force. Table 2 shows the results of this testing.

Table 2 Terfenol-D bulk motion transducer preload testing results

Preload (MPa)	Blocked force, no displacement (N)	Voltage to reach 90% saturation force	Max displacement, no load (μm)	Voltage to reach 90% saturation displacement
0.0	2759	136	104	121
1.7	3317	139	177	113
2.5	3442	140	176	116.7
3.4	3795	146	212	122.6
4.2	3358	140	190	117.8
5.1	2904	156	198	123.7
6.8	2152	158	202	137.3
8.5	2383	158	177	144.7
10.2	1412	159	142	148.7
11.9	1159	156	112	149.9
13.6	1127	160	85	149.9
15.3	864	163	69	149.9
17.0	659	166	53	149.9
18.6	429	166	46	153
20.3	382.2	163	39	154

The bare transducer was then tested to find its no-load displacement response, $x_m(V)$. Maximum no-load displacement at the transducer $x_m(V_{max})$ was 212 μm, as shown in Figure 9. Note that the output as a function of voltage is, indeed, quite nonlinear. Friction in the transducer would be most prevalent in the form of stiction, the transition from static to kinetic friction as the transducer changes directions, and would appear as a vertical discontinuity in Figure 9. Any friction effects from the transducer will be amplified by the displacement amplification system described in Chapter 3, and will be investigated in greater detail then.

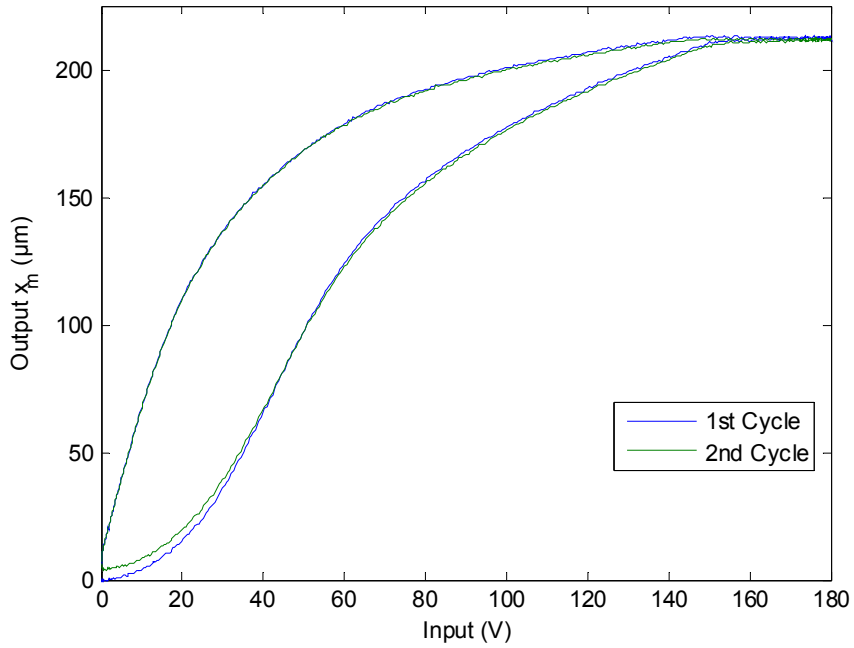

Figure 9 Terfenol-D bulk motion transducer no-load displacement output

Next the transducer's output was blocked, and maximum blocked force at zero displacement measured 3795 N. This same testing was conducted at a series of displacements throughout the transducer's travel to find the maximum blocked force throughout the transducer's travel. This testing essentially represents Equation (2), giving $F_T(V_{max})$ vs. x_T, with $x_m(V_{max})$ = 212 μm. A linear fit of this curve was applied, with the magnitude of the slope being equivalent to $k_T(V_{max})$, at 18 N/μm, as shown in Figure 10. The elastic behavior of Terfenol-D still showed some nonlinearity, even at a constant magnetic field.

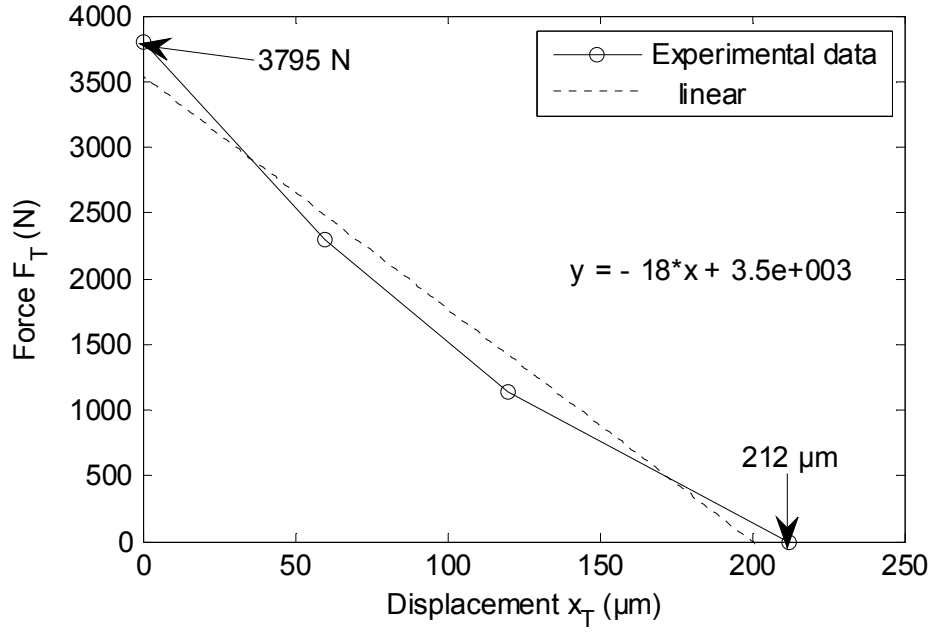

Figure 10 Blocked force and compliance testing of Terfenol-D transducer for bulk motion with linear fit used to determine effective spring stiffness

Thermal testing was conducted to examine the system response to self-heating. Coil resistance was measured at 9 Ω, so with a saturation voltage of 150 V power consumption is 2.5 kW. Hysteresis loop testing was carried out across a series of varying temperatures from 25-45º C using a 0-180V sinusoidal input with a frequency of 1 Hz. Across this range of temperatures, there was a cumulative thermal drift of 44 μm and a reduction in range of approximately 10% of overall output as shown in Table 3.

Table 3 Thermal testing results for Terfenol-D bulk motion transducer

Temperature (ºC)	Starting displacement (µm)	Ending displacement (µm)	Range (µm)
25	0	199	199
27	0	197	197
29	3	200	197
31	5.5	200	195
33	13.7	206	192
35	18.8	208	189
37	24.4	212	188
39	33.4	218	185
41	38.6	221	182
43	41.4	223	182
45	44.3	225	181
		% change:	10.1%

Compressed air cooling is used on this actuator which circulates between the coil and inside of the case. Heating of the actuator during operation causes both thermal drift and range errors. Thermal drift is simply caused by thermal expansion. One potential source of range errors is due to coil heating. Heating of the wire increases the resistivity of the wire, reducing current flow and therefore magnetic field strength for a given voltage. This effect was not present in this testing, which is not surprising given a temperature range of only 20ºC. A more likely cause of range reduction in this application is that thermal expansion results in additional spring preload in the transducer. This highlights the importance of taking effort to minimize the spring rate in the transducer's preload springs.

The system's frequency response to hysteresis was also tested by conducting hysteresis loop testing at a series of different frequencies. Testing was conducted on both the bare transducer and the full lever system to isolate the effects from each system. Hysteresis

is typically present in Terfenol-D predominantly due to lags in demagnetization in low frequencies (Dapino, 2004). Figure 11 shows the results of this testing across a range of 1-20 Hz. Magnetic hysteresis plays a role over 5 Hz. Coil impedance was also tested up to 1 kHz as assembled, with no measurable change in impedance across this range.

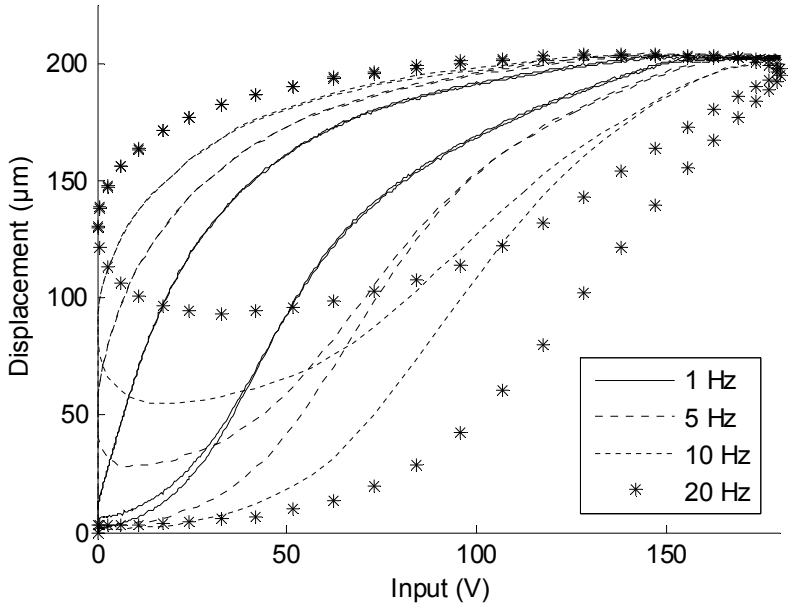

Figure 11 Hysteresis vs. frequency testing, Terfenol-D bulk motion transducer

2.6 Conclusion

Terfenol-D would appear to be well-suited to this application. Testing has shown the transducer is capable of 3.8 kN blocked force and 212 µm displacement, and no friction was perceived in this testing. Implementation is much simpler than a hydraulic or pneumatic system, and the frictionless motion allows for the high displacement resolution required for the high precision requirements of microforming. Several design considerations were taken

into account to ensure these results. An efficient magnetic path increases the efficiency of the system. Preload system design is important to ensure that the spring rate is low enough to prevent loss out output at maximum travel, and preload levels are important to find the best balance of static response and hysteresis. Intelligent choice of common assembly references prevents manufacturing tolerance stackup. Finally, ensuring that only axial loading on the rod is present not only protects the rod but eliminates friction from the output stage.

While displacement output as a function of voltage is highly nonlinear, a linear spring model used with maximum voltage magnetostriction appears to be relatively close, with an error of only 6% with regards to no-load displacement and 8% with regards to blocked force. Cooling is also a very important consideration, with a temperature increase of just 20º resulting in thermal drift of 21% of maximum travel; this can adversely affect output range as well if the preload spring rates are not sufficiently low. Hysteresis plays a minor role below 5 Hz, however range reductions of nearly 50% are present by 20 Hz. Overall transducer performance is considered satisfactory for this low-frequency, high-power application.

CHAPTER 3. DESIGN AND CHARACTERIZATION OF A DISPLACEMENT AMPLIFICATION SYSTEM FOR USE IN MICROFORMING

3.1 Nomenclature

F_T = transducer force

$k_T(V)$ = effective spring rate of transducer

$x_m(V)$ = magnetostrictive displacement

x_t = transducer displacement

F_B = force required to bend flexure joints

k_B = effective spring rate of flexure joints in bending

x_O = lever system output displacement

x_p = lever system assembly preload displacement

R = lever ratio

F_O = lever system output force

x_c = post-compliance transducer displacement

k_c = effective spring rate of lever system due to compliance

3.2 Introduction

The first step in designing the lever system to accomplish bulk motion was to select the best lever configuration. Given that (a) Terfenol-D is capable of 0.12% static magnetostriction (Dapino, 2004), (b) rods of Terfenol-D are commonly available in standard

lengths of up to about 150 mm, and (c) 2.5 mm of output displacement is desired, lever ratios should be in the range of 10-15. Rod diameter was determined by desired output force, along with lever ratio and Young's modulus of Terfenol-D in a blocked state. The following lever configurations (Figure 12) were selected for review: a conventional straight lever design, a two-section bent lever design, and a symmetric four-section bent lever design.

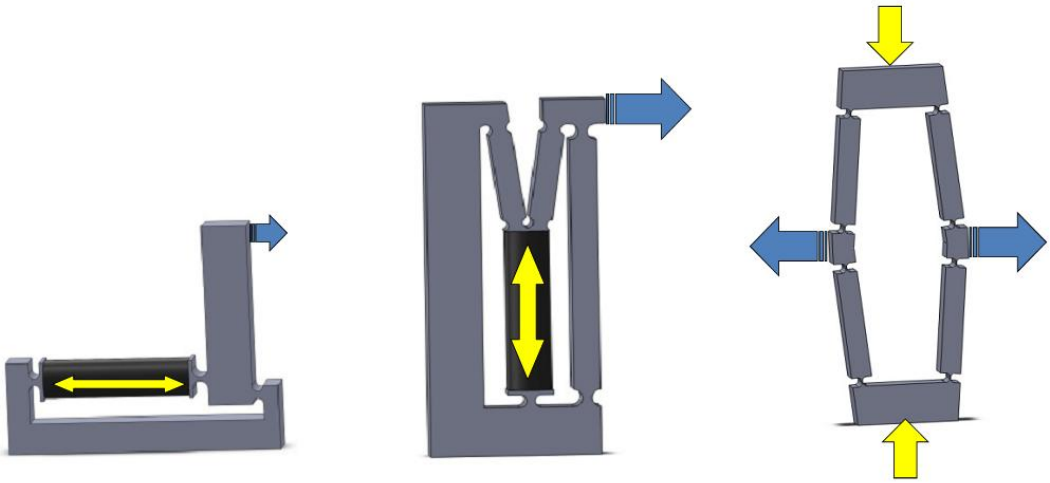

(a) (b) (c)

Figure 12 Candidates for lever system design, from left to right: (a) straight lever, (b) bent lever, (c) dual bent lever. Yellow arrows represent transducer output, blue arrows represent lever system output.

A variation of the dual bent lever design shown in Figure 12 (c) that used separate joints held in place with press-fit pins was chosen for lower cost as compared to a monolithic system cut from a large piece of billet. This design is quite similar in function to flextensional displacement amplifiers commonly used with electrostrictive or magnetostrictive transducers.

From a most basic perspective, flexure joints can be approximated by a beam in bending. A beam of regular cross-section is convenient from an analytical standpoint, but offers a huge compromise in stiffness as the compliant bending area is relatively long. Instead, circular notch hinge joints are much more popular, as they provide much larger axial stiffness by concentrating the less-stiff, bending portion to a much smaller area without creating excessive stress concentrations. Analytically they can be designed using integral methods, although FEM has become more popular in recent years. One chief advantage of flexure joints is their lack of moving parts, making them inherently devoid of friction or backlash (Kang, 2005).

The basic lever system configurations shown in Figure 12 were compared on the following bases: (1) linearity of motion, (2) size, (3) complexity, and (4) compliance. Linearity was chosen to ensure that lever ratios (or displacement gains) were relatively constant throughout the arc of travel. Size was considered because a large factor in the future marketability of this design is in the overall size of the unit, as shop floor space is always at a premium. Complexity was chosen since it generally affects both the cost and reliability of the unit. Cost was not directly considered because all designs had similar effective lever ratios, assuming rigid bodies, all designs could effectively use the same transducer which comprised the majority of the cost of the device.

Compliance was the most heavily weighted factor, as compliance not only leads to un-desirable off-axis movement in the output section, but also results in an effective "loss" of motion, as a considerable portion of the total displacement could go into compressing the

flexure joints. In effect, this would require a transducer with larger travel, increasing the cost. One key compromise in flexure joint design is obtaining high axial stiffness without excessive bending stiffness. Their axial stiffness can be tailored by angular deflection requirements. A design which has low angular deflection requirements is well-suited for a flexure joint design, as this allows thicker cross-sections in bending and therefore higher axial stiffness. However, increasing cross-sections naturally increases the bending moment, causing the flexure to act as a leaf spring, adding a resistance to motion that may be large enough to affect the overall system's motion.

3.3 Lever configuration selection

A decision matrix was used to determine which lever system would be best suited to this application. Initial flexure joint design and modeling used a simplified cantilevered beam model for comparative analysis between the configurations. The lever system configuration was then chosen based on the best combination of linearity of motion, overall size, complexity, and compliance.

3.3.1 Initial flexure joint design and modeling

For analysis, the flexure joints were modeled as rectangular cantilevered beams under axial loading, subjected to compressive axial loading and a known angular deflection that corresponds to one half of the angular travel of the system, as shown in Figure 13.

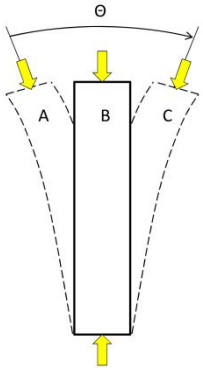

Figure 13 Rectangular cantilevered beam model of flexure joints. Beam A represents the starting position, B represents mid-travel (no bending), and C represents the ending position. The yellow arrows represent loading present.

The assembly was designed to be manufactured as it would be in the center of its linear travel (position B), and then assembled pre-loaded to position A. This way, if total angular travel for a particular joint is Θ degrees, and components are assembled to be in an initial state of -Θ/2 (position A), then maximum travel will occur at Θ/2 degrees (position C), thus effectively halving the angular deflection requirement of the joint. This scenario also maximizes linearity of motion for a consistent lever ratio.

For initial cantilevered beam analysis maximum stress was taken as the sum of axial and bending stress. A2 tool steel was chosen for the flexures due to its high strength, good fatigue life, and ability to be deep-hardened. Maximum allowable stress was determined using a factor of safety of 1.3 with respect to the endurance limit of high strength steels, resulting in a maximum allowable stress of 569 MPa.

The effects of bending moments on reducing the output force of the assembly were only calculated for the worst case to determine their significance. Joint width in its longest

dimension was fixed to 50 mm, while joint height and thickness were calculated to minimize compliance subject to stress and buckling constraints.

3.3.2 Linearity, size, and complexity

Linearity was analyzed by plotting geometric output motion vs. input motion. Designs were evaluated by creating a linear fit trend line to these plots and comparing their R-squared values. A benchmark for size was developed by creating a worst-case scenario based on the length of a direct-acting actuator. Without any mechanical advantage, given the magnetostriction and displacement considerations above, this transducer would be over 2 meters long. Complexity was simply defined as the number of beams and joints in each design.

3.3.3 Compliance

In a compliant joint design, it is desirable to have bending compliance in one direction while maintaining stiffness in all other directions. This can be attained by designing joints with large aspect ratios (Bacher, 2002), but even these designs have a limit to their effectiveness. Therefore, for a given flexure joint, compliance is primarily determined by loading and angular travel. The rest of the mechanism has significantly more design flexibility that allows designs that are sufficiently overbuilt with regards to stiffness, so compliance was evaluated only in the flexure joints for comparison purposes. Compliance was estimated by treating each joint as a simple beam in uniaxial compression using the following equation:

$$\delta = \frac{F\ell}{AE} \tag{3}$$

where δ is joint deflection, F is the applied load, ℓ is the effective length of the joint, A is the cross-sectional area of the joint, and E is Young's modulus. Total effective deflection for each design was calculated by taking the sum of every joint's deflection times each joint location's effective lever ratio, using the following equation:

$$\delta_{total} = \sum_{j=1}^{n} \delta_j R_j \tag{4}$$

where δ_{total} is total deflection, and δ_j and R_j are the deflection and effective lever ratio at each joint location.

3.3.4 Lever configuration selection

The first stage of analysis involved determining which factors were important. The effects of flexure joint bending moments in the design with the largest bending moments, the straight lever system, resulted in a reduction of force of 0.1 N at the output stage for the cantilevered beam approximation. Therefore the effects of bending moments in the flexures were neglected for the remaining studies. In the linearity study, all three designs had R-squared values greater than 0.999, so linearity was considered a non-determining factor. This is expected, as the relatively small overall travel resulted in angular travels of the flexure joints of well under 1 degree from the center of travel. The effects of the remaining factors, size, complexity, and compliance, were analyzed using a decision matrix with weightings of 20% for both size and complexity and 60% for compliance. Table 4 shows the raw values for each of these factors for each design.

Table 4 Raw (unweighted) values for factors influencing design decision.

Design	Compliance (m)	Size (mm)	Complexity (# of features)
Straight Lever	6.92E-05	300.0	5
Bent Lever	3.62E-04	261.7	11
Dual Bent Lever	2.23E-07	442.4	14

To get a final weighted score the results were scaled by their respective weighting factors such that a maximum of 10 points were available for a given design (0-6 for compliance, 0-2 for size, and 0-2 for complexity). For compliance, a score of 0 corresponded to a compliance equal to 5% of the overall travel, while 6 points corresponded to the lowest compliance of all designs which was less than 0.009%. Note that designs with greater than 5% compliance receive negative points. This simulates an additional cost criterion, as designs with excessive compliance will require a larger, more expensive Terfenol-D transducer to achieve the same motion. For size, a score of 0 corresponded to half of the overall length of a design with no mechanical advantage (1560 mm), while 2 corresponds with the smallest of all designs which was 262 mm. For complexity, the design with the highest number of features gets 0 points, while the one with the lowest number of features gets 2 points. Table 5 shows the final weighted scores for the designs, with the dual bent lever design as the highest rated design. One additional advantage of the dual bent lever design over the others is that despite being complex, it has symmetry over two planes, which should practically eliminate off-axis motion.

Table 5 Final values for design decision matrix.

Design	Compliance	Size	Complexity	Total
Straight Lever	2.7	1.9	2.0	6.5
Bent Lever	-11.4	2.0	0.7	-8.7
Dual Bent Lever	6.0	1.3	0.0	7.3

3.4 Lever system design

After selecting the most appropriate lever configuration, a circular hinge model was designed using COMSOL. Figure 14 shows the layout of the various components for the first iteration of the bulk motion system. One departure from typical flextensional style designs is the use of detachable joints which were used to reduce cost as compared to monolithic block designs wire EDM cut from a single billet.

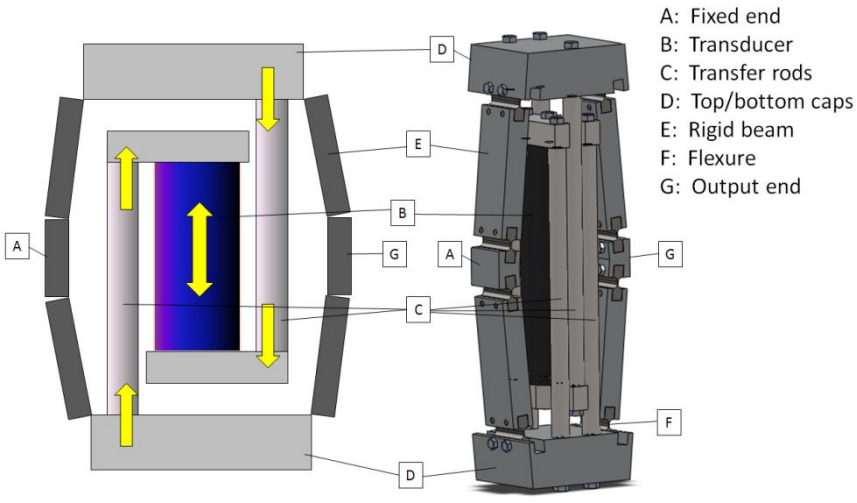

Figure 14 Complete bulk motion assembly

The principle of operation is as follows: The assembly is fixed at (A). The Terfenol-D transducer (B) expands longitudinally due to magnetostriction, causing the transducer end caps to move away from each other. The transfer rods (C) serve the purpose of changing the

direction of the applied force from the transducer, as they are attached to opposite top/bottom caps (D). This, in turn, causes the top and bottom caps to move closer to each other, thus horizontally expanding the outer frame which is made up of rigid beams and flexure joints (E, F). Due to the geometry of the outer frame, displacement at the output (G) is increased by a factor of about 11. Backlash is essentially eliminated in shear joints by using press-fit pins or centerless ground AN bolts in close-fit holes when required.

The lever system's operation was validated via a 2D plane strain study using COMSOL. This ensured that not only was stress within allowable limits, but also that the flexure joints were behaving as expected. Figure 15 shows the von Mises stress results of the FEM analysis for the fully loaded condition.

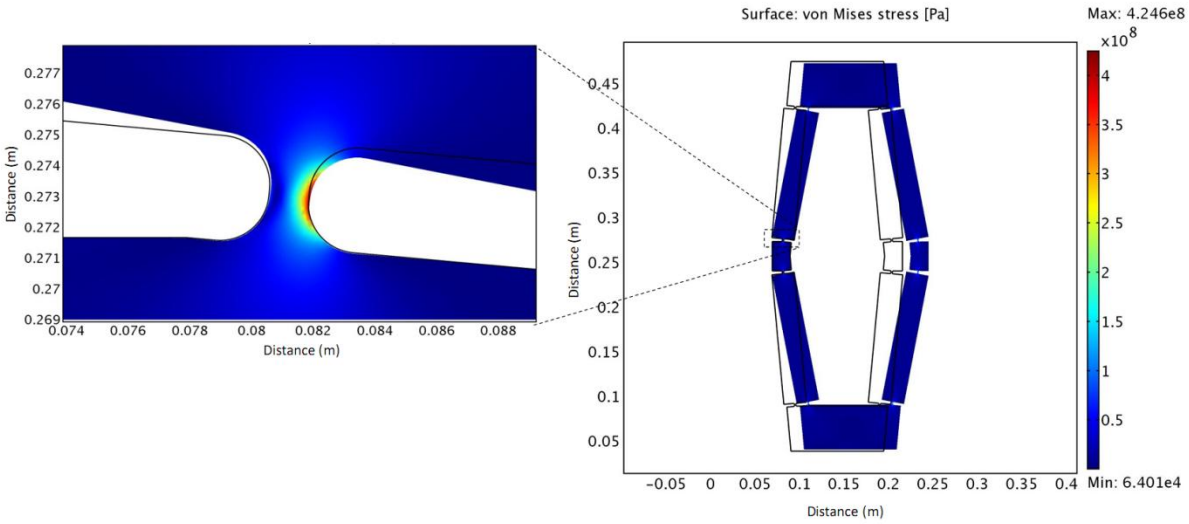

Figure 15 FEM von Mises stress results for second iteration flexure joint design.

3.5 Lever system model

The system can be modeled as a collection of springs. The linear spring model of the Terfenol-D transducer outlined in Chapter 2 is used here as well, although a more

comprehensive model for intermediate voltages could be substituted if necessary. Each flexure joint (Figure 14, item *F*) also acts as a leaf spring that acts on the effective axis of bending, which applies a bending moment to all the elements in the lever system purely as a function of output displacement, independent of load. This is minimized by assembling the lever system as shown in Figure 13, where the bending moment is zero at mid-stroke. The entire system has a compliance which acts as a simple linear spring with a measurable stiffness and deflection that occurs purely as a function of loading at the output stage, independent of displacement.

Figure 16 shows a complete simplified model of the lever system. While much simpler than the model given in Figure 14, it is functionally equivalent with a lever ratio, *R* defined as *h*/*g*.

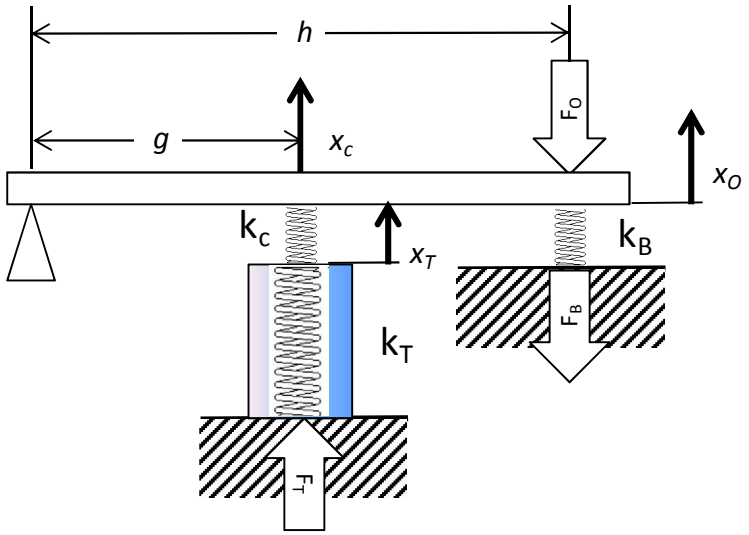

Figure 16 Spring model of lever system

There is a resistance to bending in each joint as it flexes throughout the range of travel. This is most simply modeled by examining the cumulative effect of all of the joints as seen at the output of the lever system, using spring rate k_B. The force required to bend the flexure joints, F_B varies purely as a function of output displacement x_O. Note also that because the transducer is installed into the lever system with a given preload so that the lever system is at position A in Figure 13, there is a given preload x_p in the effective flexure bending spring k_B. This system was assembled with a preload x_p of 800 μm. The force resulting from the bending moment in the flexures, F_B is given as:

$$F_B = k_B(x_O - x_p) \tag{5}$$

The output force of the system, F_O, can be found by summing the moments about the far-left pivot, where counter-clockwise forces are positive:

$$\sum M = 0 = \frac{F_T}{R} - F_O - F_B \tag{6}$$

System axial stiffness is represented by k_c; its effects are seen as a reduction in total displacement x_O under load, and it acts as a linear spring in series with the transducer. This model clarifies the requirement for high axial stiffness in the joint, as any deflection in k_c reduces the overall displacement output of the system at a given load. The displacement output of the system after taking compliance into consideration is simply the output displacement divided by the lever ratio:

$$x_c = \frac{x_O}{R} \tag{7}$$

The displacement lost due to compliance can be expressed as:

$$x_T - x_c = \frac{F_T}{k_c} \tag{8}$$

Algebraically combining these force-distance relationships it is possible to predict the available output force as a function of displacement:

$$F_O = \frac{k_T(V)x_m(V) - \dfrac{k_T(V)x_O}{R}}{R\left(1 + \dfrac{k_T(V)}{k_c}\right)} - k_B\left(x_O - x_p\right) \tag{9}$$

3.6 Determination of model parameters

Figure 17 shows the complete Terfenol-D powered bulk motion system. The experimental setup used for testing was the same outlined in Chapter 2.

Figure 17 Complete Terfenol-D powered bulk motion assembly

A multi-piece flextensional lever system could reduce cost, especially on a system as large as this, but has other inherent drawbacks that can be difficult to overcome. Using separate joints and beam elements results in many interfaces between components, which results in a large degree of manufacturing tolerance stackup around the loop constructed by the lever system. On this system, upon initial assembly with randomly chosen and oriented components, there was an approximately 5 mm offset to bridge when bolting the final joint connection together. Aside from difficult assembly, this causes binding in the flexure joints as the axes of the flexure joints are no longer parallel, forcing bending to occur on an axis that is offset from the preferred "weak" axis of bending. This tends to increase the spring

rate due to joint bending, k_b. For this research the lever system was "blueprinted" by measuring the manufacturing error at each joint and then matching components so the tolerances would come as close to cancelling each other as possible. Despite the extra effort required, a primary benefit to using bolt-on connections is that the can be easily replaced. This is not only convenient in the event a joint is damaged, but also allows for much cheaper experimentation with different joint geometry.

The lever ratio was tested directly by measuring the displacements of the output and one of the end caps (D in Figure 14). A linear fit of the plot of these two displacements under no load testing (Figure 18) yielded a slope of 10. This differs by 10% from the geometric lever ratio of 11, which assumes pin pivots at the center of each flexure joint. The mechanism for this reduction is unclear, although it could possibly be attributed to complex stress distributions due to these flexure joints being relatively thick. Thickness to fillet ratios (t/R) for typical circular hinge flexure joints fall in the range of 0.05-0.8(Yong, 2008), while the joints in this design have a t/R ratio of 1.3.

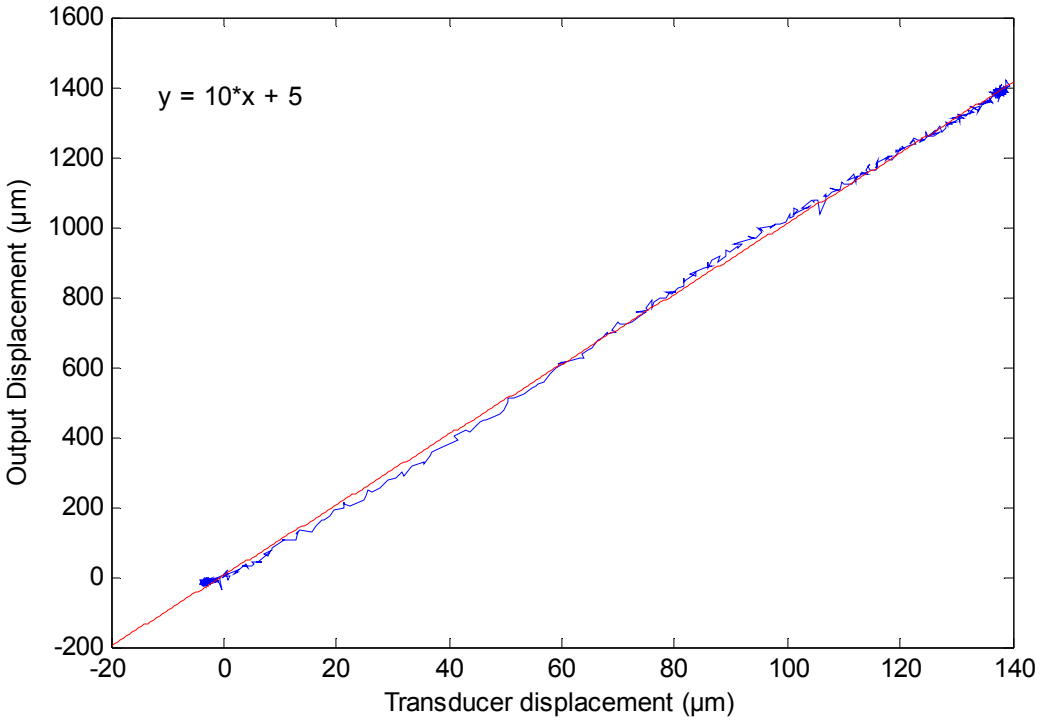

Figure 18 Lever ratio testing. The system was run through maximum displacement without load, and the output displacement was measured as a function of transducer displacement.

Next the bending stiffness of the flexure joints was measured to find k_B. The lever system, without transducer, was moved by hand, and force and displacement were measured. As expected, the output was very linear. A linear curve fit yielded an effective spring rate, k_B of 0.073 N/µm, as shown in Figure 19.

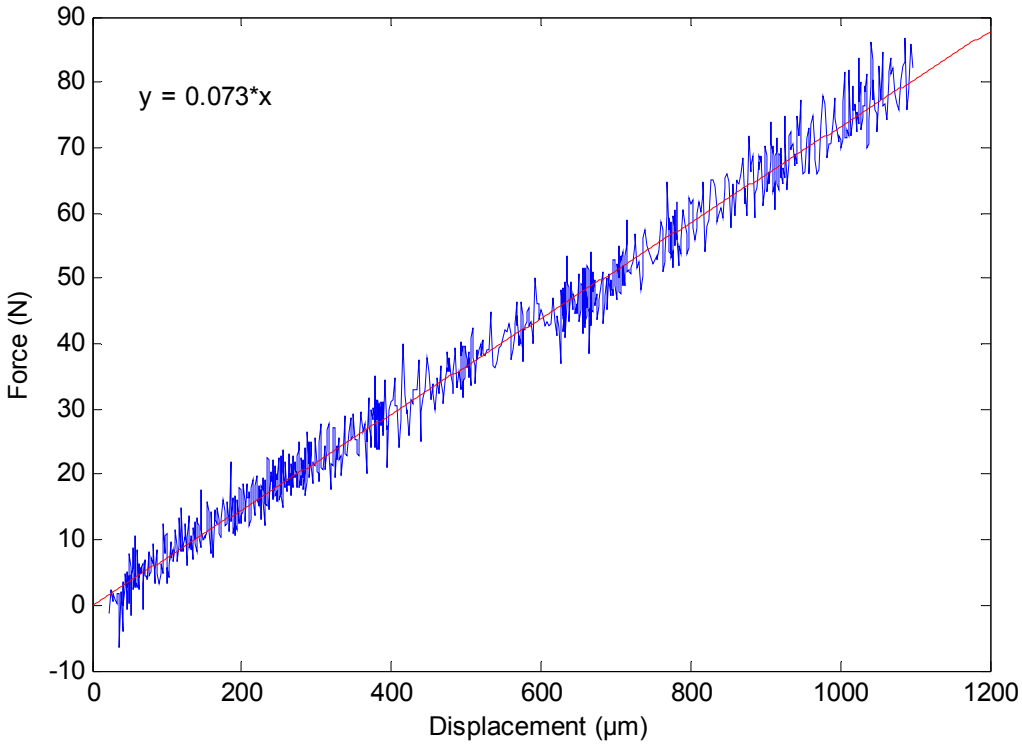

Figure 19 Manual testing used to determine effective bending spring rate of flexures. Force required to move lever system at its output was measured as a function of displacement, also measured at the output.

Lever system compliance k_c was measured directly by measuring transducer displacement in the fully assembled lever system relative to output force under full load. The output displacement x_O was blocked and transducer displacement x_T was measured as a function of F_O. With x_O blocked, x_c is assumed to be zero, and $F_T = F_O*R$. With the relationship given by Equation (8), k_c can then be found by taking the slope of F_T vs. x_T, which was found to be 44 N/μm as shown in Figure 20.

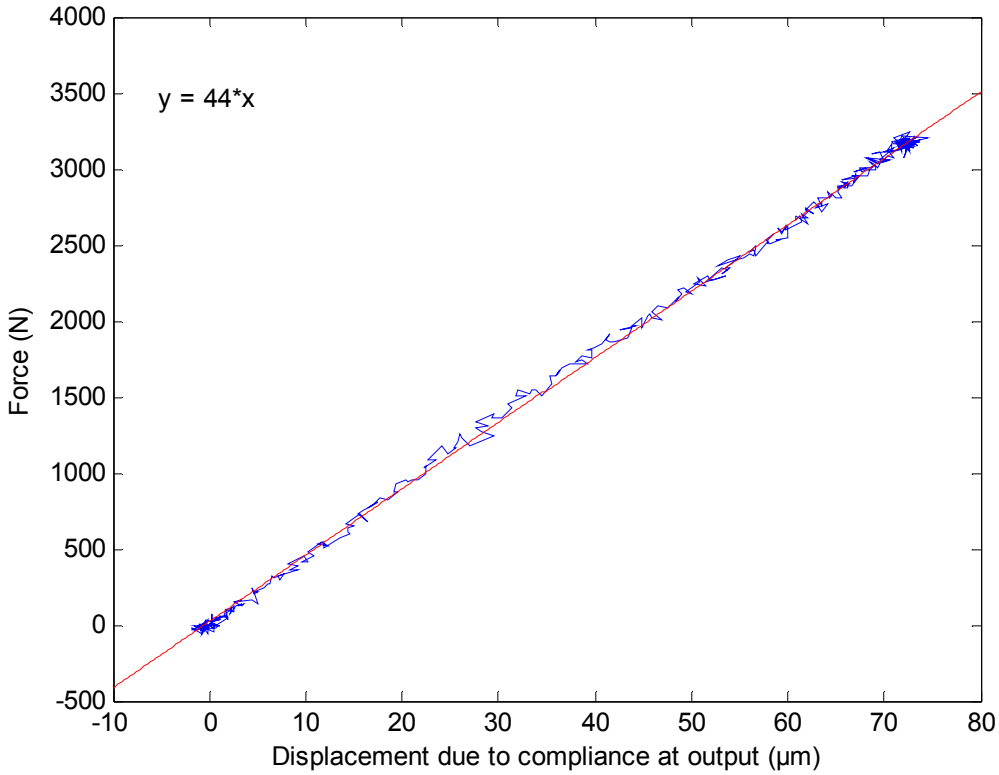

Figure 20 Lever system compliance measurement. The system's output displacement was blocked, and transducer displacement was measured and then scaled by the lever ratio to find force as a function of displacement due to compliance at the output.

3.7 Model validation and other testing

To validate the model given by Equation (9), blocked force F_O vs. displacement x_O was tested by measuring the force available at V_{max} at a series of different displacements throughout the lever system's range. A comparison of the model with experimental data is given in Figure 21. Aside from the same nonlinearity encountered while determining k_T, the results overlay quite well, with a maximum error of 11% with regards to blocked force and

an error of only 2% for predicted free displacement. The measured maximum blocked force for the lever system measured 365 N, and maximum free displacement measured 1600 μm.

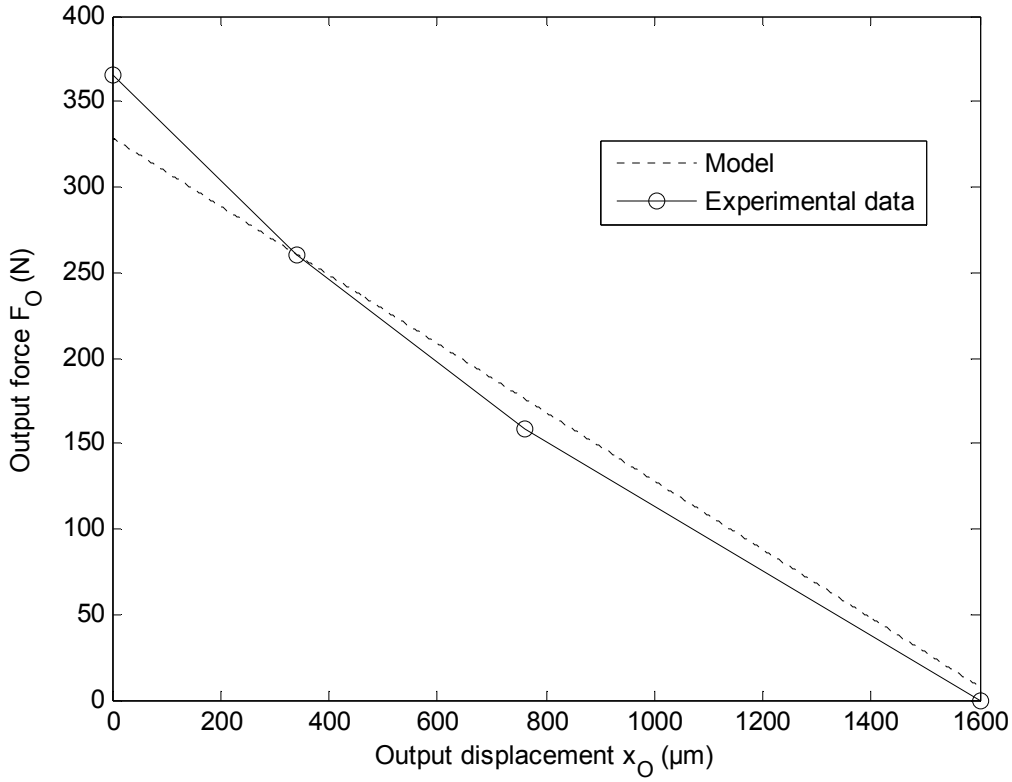

Figure 21 System maximum output force vs. displacement model compared to experimental testing

Exploring the model allows a very convenient method to optimize a design towards either force or displacement. An upper limit for flexure joint performance can be found by setting k_c to a very large number and k_B to a very small number, as this would represent joints that are nearly rigid axially with almost no bending resistance. Increasing k_c by three orders of magnitude and decreasing k_B by three orders of magnitude yields a predicted maximum

force of 382 N, a 5% improvement, and a maximum displacement of 2100 μm, a 31% improvement.

Due to the assistive loading provided by the flexure joints as they move from position *A*-*B* in Fig. 3, some interesting results can be obtained by experimenting with the independent effects of k_B and k_c. Doubling both k_c and k_B results in a maximum force of 433 N, an 18% improvement, and a maximum displacement of 1470 μm, a compromise of only 9%.

Resolution testing took a closer examination at any possible effects of friction and backlash, as well as helped to determine the smallest step the system could reliably make. A 1V amplitude square wave was superimposed on a 40V DC signal to determine the effects of changing direction repeatedly at a very small displacement. This should exaggerate any effects of backlash.

Figure 22 shows the results of this testing. The capacitive displacement sensor was used for this testing with a low-pass filter set at 5 Hz. Even with aggressive filtering the system limitation appears to be in measurement, primarily in noise. Measurement resolution of less than 1 μm was achievable with consistent system output. A slight upward trend can be seen due to thermal effects, as the testing was conducted over a relatively long period of time to minimize the effects of aggressive filtering.

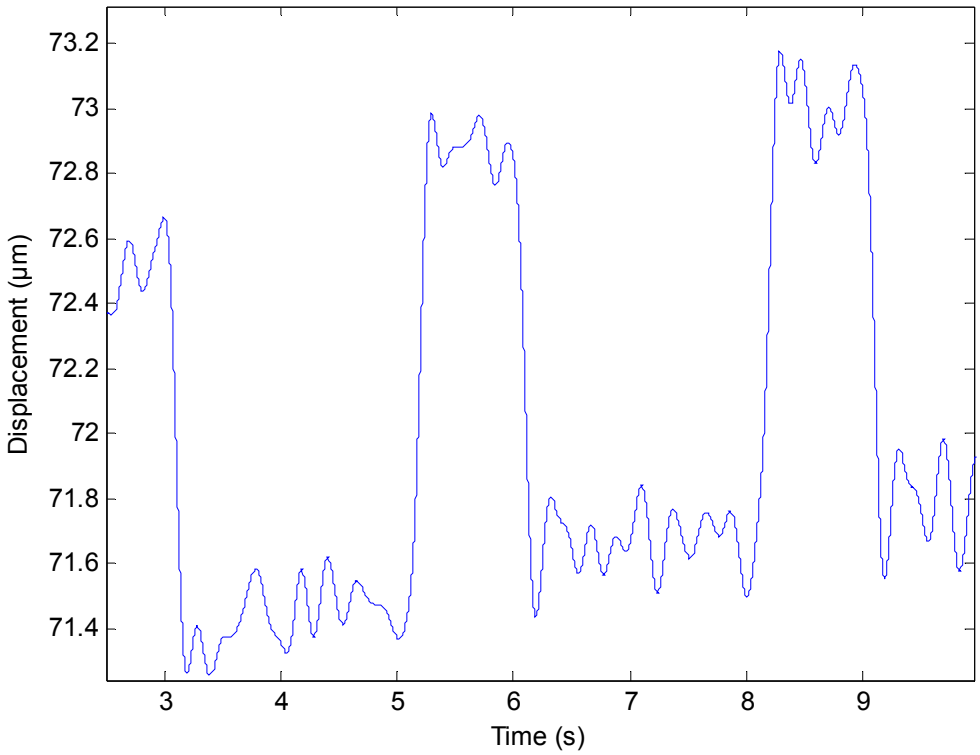

Figure 22 Resolution testing consisting of superimposing a 1V square wave on a 40V DC signal. Filtering set at 5 Hz to reduce measurement noise.

Hysteresis vs. frequency testing was conducted on the full system in the same manner as on the bare transducer as in Chapter 2. Figure 23 shows the results of this testing. Inertial effects become clear in the full system testing, with overshoot beyond maximum static displacement appearing near and over the system's resonant frequency. Inertial effects are also present in the broadening of the hysteresis loop, as the mechanical system lags the electrical input. Mechanical resonance occurs at approximately 35 rad/s, or about 5.6 Hz. This equates to a maximum no-load speed of 9 mm/s, given a no-load range of 1600 µm.

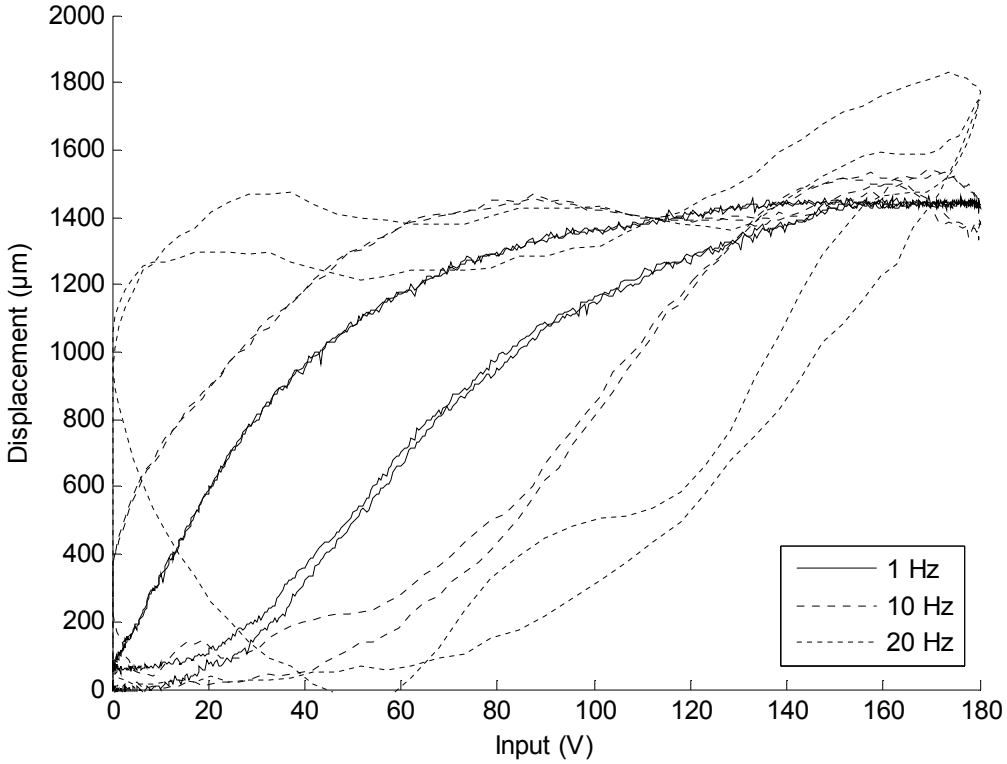

Figure 23 Hysteresis vs. frequency for full microforming system.

3.8 Conclusion

The simple linear model presented here provides an adequate prediction of force and displacement attainable for a given transducer and lever system. Flexure joint design requires a tradeoff between force and displacement in that stiffer joints typically give both a larger k_c and k_B. Due to the complexity of the relationships between these factors, this problem is well suited to a numerical optimization.

System resolution exceeded measurement capabilities and appears to be well under 1 µm. However, as can be seen from Figure 22, with a mean voltage of 40V the system

experienced approximately 0.5 μm of thermal drift over a period of 6 seconds. This system used simple air cooling, although liquid cooling would provide much more temperature stability and is recommended for duty cycles greater than 10%.

Both the transducer and the full lever system begin to show errors at frequencies over 5 Hz. While this system is not designed for cyclic operation, frequency response is useful to get an idea of what speeds are attainable by the system as well as its limitations.

CHAPTER 4. EXPERIMENTS AND ANALYSIS IN ULTRASONIC-ASSISTED PUNCHING IN ALUMINUM

4.1 Introduction

Ultrasonic-assisted forming has seen a good deal of research since the 1950s (Blaha and Langenecker, 1955) with a recent resurgence due to the advent of low cost ultrasonic generators. Industrial applications are limited but have existed since the early 1970s in wire drawing (Langenecker, 1981) and tube bending (Langenecker, 1973), although the most promise in ultrasonic-assisted forming is in helping overcome some of the particular challenges of microforming (Engel, 2002). Ultrasonic-assisted forming is carried out by applying vibration to forming dies during deformation, using frequencies in the range of kilohertz, and displacements in the range of micrometers. This results in a measurable reduction in friction (Ngaile, 2008) and improvement in surface finish (Devine, 1981), as well as a significant reduction in forming stress (Culp, 1973) and increase in plasticity (Jimma, 1998). The reduction in forming stress and corresponding increase in plasticity has proven especially helpful in increasing the usable drawing ratios in wire and tube drawing (Siegert, 2001).

Much research has also been conducted recently to characterize ultrasonic softening during plastic deformation (Yao, 2012a) and its effect during many forming processes involving plastic deformation including micro-extrusion (Ngaile, 2008), deep-drawing (Jimma, 1998), sheet bending (Devine, 1981), and wire drawing (Siegert, 1996). On the

other hand, there is little to no research involving ultrasonic-assisted fracture or ultrasonic-assisted manufacturing processes that involve fracture such as punching or blanking, which will be the focus of this paper. In this study, the effects of punching speed and ultrasonic intensity on punching force and fracture surface have been analyzed. After background information on punching operation, experimental procedures are described. The punching results are then compared with a control group with no vibration.

4.2 Background

Punching or blanking is considered a mature, well-known process, although there is still recent research conducted on process improvements to improve surface finish and minimize burrs (Li, 2002).

Punching force can be estimated based on the ultimate tensile strength of a material as the process is carried out to complete fracture. This is multiplied by the overall shear area undergoing punching, which is simply the product of the sheet thickness and perimeter (Kalpakjian, 2003). A cross-section of a typical punching specimen with all important parameters is shown in Figure 24. During the punching process, the material goes through several stages. After the initial force buildup in the linear elastic region, the slope of the curve levels out as plastic deformation occurs. The shiny, burnished portion of the sample is created during this phase of deformation, which occurs in an area of intense shear strain. As plastic deformation continues, crack propagation begins at the upper and lower portions of the highly strained area. The rough fracture surface forms during this phase of deformation, ultimately ending in fast fracture.

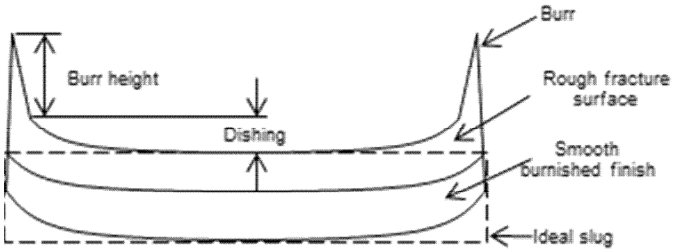

Figure 24 Punching features and parameters

Recent punching research has shown that a primary factor affecting the height of the burnish band is punch clearance, with smaller punch clearances resulting in larger burnish bands (Lo, 2010). Thermal effects are also known to occur as a function of strain rate during processes with highly localized shear. When strain rates increase, thermal effects of deformation do not have time to conduct to adjacent material. This results in a condition that approaches an adiabatic band, where thermal effects result in a significant increase in flow stress (Hayden, 1965). In tempered alloys such as tool steel, deformation energy causes localized heating that can result in a reduced flow stress and increased ductility with increasing strain rate (Becze, 2001), while materials with fewer dislocation barriers such as annealed aluminum 1100 or zinc show an opposite adiabatic cooling effect with increasing strain rate (Stevenson, 1999), with an increase in punching force of approximately 30% when punching speeds increase from $14.7(10^{-7})$ to 19.5 m/s, as shown in Figure 25 (Blazynski, 1987).

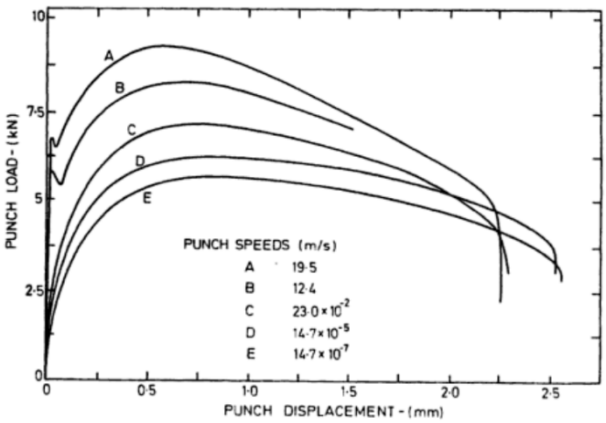

Figure 25 Speed effect on punching in 1100-O aluminum (Blazynski, 1987)

While softening due to localized heating is intuitive, localized cooling requires an explanation based on surface energy. As individual grains are deformed during punching, their shape changes from spheroidal to greatly elongated, resulting in a significant increase in surface area for a particular grain. From a fracture mechanics standpoint, a significant amount of energy is required to develop these free surfaces, resulting in a localized drop in temperature. The accompanying reduction in lattice vibration results in a measurable stiffening of the material with increasing strain rate (Blazynski, 1987).

Several benefits of ultrasonic-assisted forming have been documented, including a reduction in friction and multiple softening modes, comprised of stress superposition and acoustoplastic softening. Friction reduction during ultrasonic-assisted forming can be explained by a transition from a stick-smear to a stick-slip phenomenon (Ngaile, 2008), while stress reduction and increases in plasticity have been explained by stress superimposition and acoustoplastic softening. The stress superposition effect works by examining the combined stress state from the sum of vibratory stress and forming stress (Malygin, 2000). The

addition of vibratory stress pushes the material to a state of higher combined stress, resulting in a reduction in mean forming stress (Daud, 2007). This effect does not occur at the microstructural level, and can even be observed in finite element modeling that uses a conventional plastic deformation material model (Hayashi, 2003).

The stress superposition mechanism does not account fully for the stress reduction observed in ultrasonic softening. An additional mechanism of acoustoplastic softening that can be explained by an increase in dislocation mobility during the application of ultrasonic vibration (Baker, 1967) has been suggested for acoustoplastic softening. This effect has also been verified by experiments that examined the internal damping of materials undergoing ultrasonic softening, which displayed that the softening occurred as a result of irreversible energy transfer caused by mobilizing medium to long range dislocation motion (Sapozhnikov, 1997).

Several of the references cited in this paper display ultrasonic softening on the order of up to 70% depending on the material. This softening appears immediately upon application of vibration, regardless of whether the sample is in a state of elastic or plastic stress, and stops immediately upon the removal of vibration (Malygin, 2000). To give further support to the theory that the softening is caused by dislocation mobility, there is also an acoustoplastic hardening effect, similar to work hardening, which remains after the removal of vibration. This effect is displayed in Figure 26 (Yao, 2012a). It is critical to note that the softening effect is only apparent during the application of vibration, while hardening effects are smaller in magnitude and permanent.

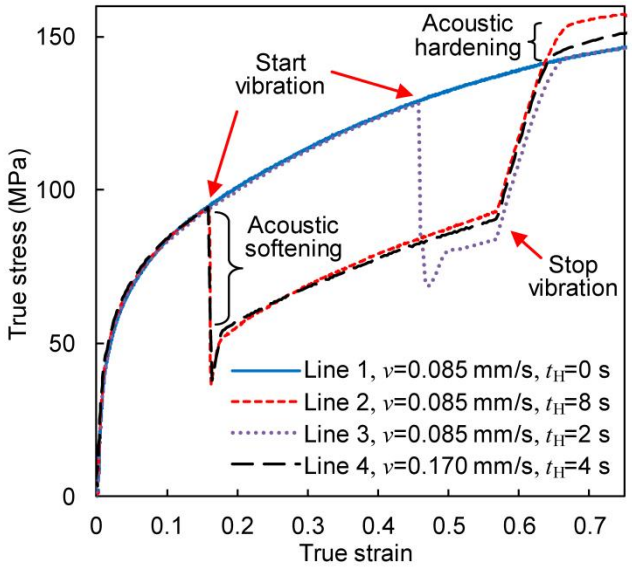

Figure 26 Acoustic softening and residual hardening present in upsetting experiments with Al 1100-O (Yao, 2012a)

This effect has a saturation level, similarly to work hardening, where dislocation density is at a maximum and no more hardening can occur, although softening is still present during vibration. While much is now known about the acoustoplastic softening mechanism, there is very little known on how ultrasonic softening affects fracture behavior, which determines not only the work required to complete the punching operation, but also the fraction of burnished to fracture surfaces present on the samples.

Ultrasonic softening has been modeled similarly to thermal softening using an Arrhenius equation (Yao, 2012b). While the effect behaves similarly to thermal effects (Langenecker, 1966), no considerable heating has been measured (Yao, 2012b). Additionally, no relative motion between the horn and work piece has been observed, which eliminates the possibility of the coulomb heating present in ultrasonic welding. Finally, the

immediate softening response to the application and removal of vibration is apparent, whereas a truly thermal process is expected to display a lagging first order system response.

4.3 Experimental setup

The punching system consists of an Etrema Products CU-18 ultrasonic transducer mounted to a sled driven by a screw, where the tuned ultrasonic horn tip acts as a punch that aligns with a modular die system. The die system has a series of holes precisely reamed to ensure a 10% punching clearance for all thickness of materials used. A frequency of 9.6 kHz was chosen to activate the transverse vibration mode in the ultrasonic horn tip, as this mode provided the largest degree of ultrasonic softening. The vibration modes and resulting magnitude and direction have been found to be very important during ultrasonic forming (Lucas, 1996), while the materials themselves are relatively insensitive to frequency (Langenecker, 1966). For this reason, only one frequency was used.

Figure 27 shows these components in detail. Sled displacement is measured by a non-contact laser displacement sensor, and punching force is measured by a force transducer sandwiched between the punching die and the back stop.

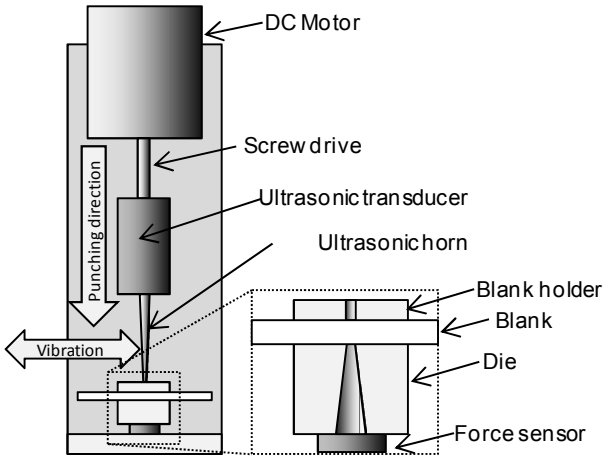

Figure 27 Details of ultrasonic-assisted punching system

Punching experiments were carried out on 800 μm thick sheets of commercial purity 1100-O aluminum at two different speeds in order to examine the effects of punching speed. Three different ultrasonic intensities were chosen that provided transverse vibration amplitudes of 2.2, 3.3, and 4.5 μm, as well as a control group with no vibration.

4.4 Results

Softening of up to 30% was observed as seen in Figure 28. Comparing the punching results at the two speeds, the most important feature is that strain rate hardening appeared between the two speeds in the control measurements, with more than 10% higher punching force and 20% reduction in displacement to fracture present based on punch speed alone. The addition of vibration to this process practically eliminated this effect, yielding results similar to those seen at the lower punching speed at the two lower vibration amplitudes, and an even higher level of softening than any other test configuration at the largest vibration amplitude.

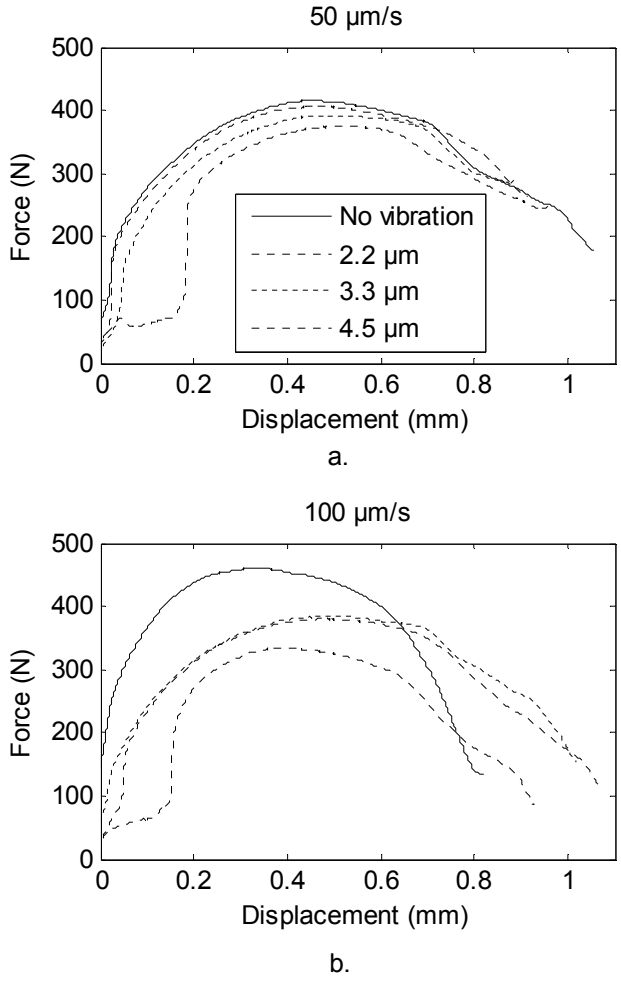

Figure 28 Force vs. displacement profiles for 800 µm thick 1100-O for punching speeds of 50 µm/s (a.) and 100 µm/s (b.) at four vibration intensities.

The results shown in Figure 28 are for one representative set of tests. All data for 1100-O were compiled to examine the overall effect of ultrasonic softening on punching force, with the results shown in Figure 29 including error bars to denote one standard deviation. From Figure 29, it is apparent that the overall sensitivity of punching force to ultrasonic vibration is noticeably larger at the higher punching speed.

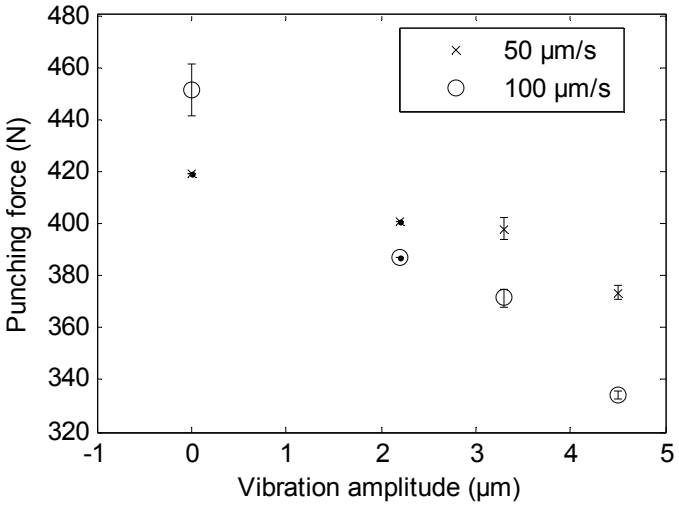

Figure 29 Punching force as a function of ultrasonic vibration amplitude for 800 μm 1100-O.

In order to get a better picture of the relative ductility of the processes, the burnished area of the sheared edges was measured. The ratio of fracture surface was measured as the proportion of punched surface that consisted of rough, fast fracture surface to smooth, burnished finish as shown in Figure 30. It is worth noting that there is some amount of inconsistency in this measurement at different points; to accommodate this 10 measurements were made across the width of the sample and then averaged.

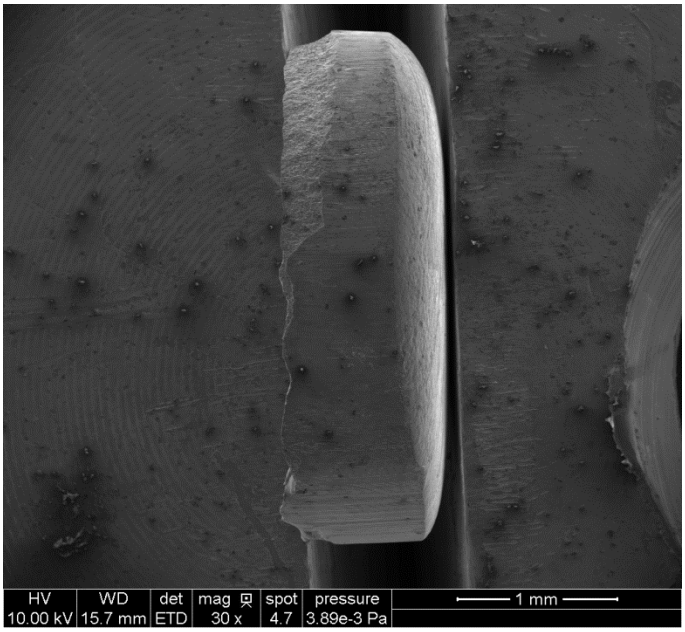

Figure 30 SEM view of punched surface, showing fractured and burnished areas.

1100-O showed a significant reduction in the proportion of fracture surface present, from 43% to 24% at the lower 50 µm/s speed as shown in Figure 31. While a significant effect on ductility was exhibited at the lower speed, almost no effect was seen at the higher punching speed.

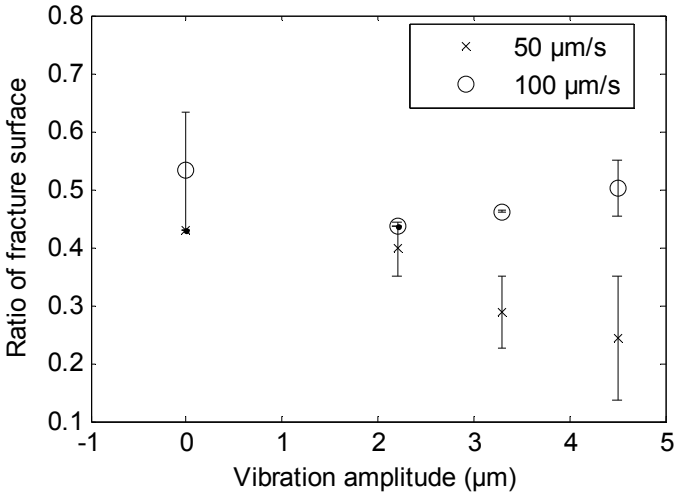

Figure 31 Ratio of fracture surface as a function of ultrasonic vibration amplitude for 800 μm 1100-O.

4.5 Discussion

The behavior exhibited in Figure 28 displays that not only is acoustoplastic softening functionally similar to thermal effects, but that the lattice vibration directly applied during ultrasonic-assisted forming can actually negate the thermal effects present due to strain rate sensitivity. The connection is quite clear when considering that the primary cause of strain rate hardening is a decline in dislocation mobility caused by a decline in thermal vibrations in adiabatic zones (Blazynski, 1987), while the primary softening mechanism present in acoustoplastic softening is caused by an increase in medium to long-range dislocation mobility caused by directly applied vibration (Sapozhnikov, 1997).

The speed effects exhibited in the non-vibrated samples in Figure 28 are similar to those shown in Figure 25, particularly in the overall shapes of the curves. Interestingly, all of the vibrated samples in Figure 28a, the 50 μm/s case, as well as the two samples with lower

levels of vibration in Figure 28b, the 100 μm/s case were similar to the non-vibrated 50 μm/s non-vibrated sample in Figure 28a. It is apparent that for a punching operation with transverse vibration, moderate vibration can negate speed effects. What is most interesting, however, is the largest vibration amplitude with high punching speed sample in Figure 28b. It bears the same qualitative shape as its corresponding non-vibrated sample, with a maximum force occurring earlier and sloping off more sharply and lower displacement to fracture, but also a greater degree of softening than any other configuration. It is not clear why this greater level of softening was not present in the lower punching speed, high vibration amplitude sample in Figure 28a, although this is hypothesized be caused somewhat by the competing effect of acoustoplastic hardening caused by a much larger cumulative exposure to vibration, similarly to that exhibited in Figure 26. This idea of competing factors is also supported by Figure 29, which clarifies the trends in reduced vibration amplitude sensitivity present at lower punching speeds. Therefore it is also hypothesized that the greater softening present in the largest vibration amplitude, highest punching speed sample relative to its lower punching speed counterpart is due to a relative lack of acoustoplastic hardening.

The comparisons in ductility shown in Figure 31 provide more insight to this phenomenon. While the effect of vibration appeared to have limited net effect on punching forces, increasing vibration amplitude did improve overall ductility; the overall effect of acoustoplastic softening did result in increased plasticity, even if overall observed punching forces were not affected significantly. Finally, the similar shapes in punching force profiles

between the no vibration and large vibration samples in Figure 28b are reflected in similar ductilities in Figure 31. In this configuration it appears that the acoustoplastic softening impacted punching force to a greater extent than plasticity.

4.6 Conclusions

In this study the effect of ultrasonic softening was examined in a punching operation, making it the first known research to examine the effect of ultrasonic softening on fracture. The effects of punching speed and vibration amplitude on punching force and displacement were inspected, as well as the proportion of rough fracture to burnished areas. Competing mechanisms appear to be at play between adiabatic strain rate effects and acoustoplastic softening and hardening effects. While adiabatic strain rate factors can be more than offset by the increased dislocation mobility brought by acoustoplastic softening, acoustic hardening can accumulate at lower speeds where adiabatic strain rate effects are less pronounced. However, in these cases acoustoplastic softening can still result in increased plasticity to fracture, resulting in a smaller proportion of fracture to burnished areas.

CHAPTER 5. THE EFFECT OF WAVEFORM ON POLYMER VIBRATION WELDING IN ABS PLASTIC

5.1 Introduction

Polymer welding using vibration energy is currently a mature and widely adopted technology. Its popularity can be attributed to the ability to achieve strengths at or near that of base materials with cycle times on the order of seconds with little to no surface preparation and a very small heat affected zone that results in high energy efficiency and minimal distortion. Vibration welding and ultrasonic welding are functionally very similar processes, both working by generating heat at the joint first through coulomb friction heating followed by viscoelastic heating (Stokes, 1988a; Zhang, 2009), with the primary differences being in the amplitudes and frequencies used and direction of vibration. Vibration welding typically operates with vibration amplitudes in the range of millimeters at 25-500 Hz using transverse vibration (Stokes, 1988a), and ultrasonic welding typically operates with vibration amplitudes in the range of micrometers at 20 kHz or more using longitudinal vibration (Benatar, 1989b). Ultrasonic welding typically uses designed energy directors at the weld joints, while vibration welding does not.

Typical control mechanisms include input energy, displacement or penetration, trigger force for activating vibration, and simple time control (Nonhof, 1996). Process optimization of these control mechanisms has been investigated as well (Van Wijk, 1996), and more advanced methods that have been researched include using amplitude and force

profiling to increase strength and reduce weld times (Grewell, 1996) and monitoring vibration transducer input impedance signatures to achieve non-destructive quality control in ultrasonic welding processes (Ling, 2006). Novel applications include microfluidic sensors and actuators for biological applications, with ultrasonic welding being especially attractive for its use of non-reactive materials and avoidance of potentially hazardous or reactive adhesives (Truckenmüller, 2006).

Research has also been conducted on not only frequency effects (Benatar, 1989b), but also the effect of welding with multiple harmonics in use simultaneously, which resulted in a larger effective weld area and weld strength (Tsujino, 2004). Strong frequency effects are also seen in far-field welding of semicrystalline polymers, where it has been found that locating weld joints at vibration anti-nodes can have a significant impact on weld quality (Benatar, 1989a).

Basic Fourier analysis reveals that a non-sinusoidal waveform can be represented as a superposition of sinusoids of varying frequencies and amplitudes. Functionally speaking, triangle or square waves are composed of several harmonics. The frequency compositions of triangle and square waves are shown up to 100 kHz in Figure 32. From here it is seen that for a square wave the fundamental frequency is of 27% higher magnitude than unity, with higher order harmonics falling off quickly in magnitude. For triangle waves, the first harmonic does not occur until 29 kHz, with all harmonics having a much lower magnitude and alternating signs. It is hoped that the broader spectrum of frequencies encountered with

these varying waveforms will result in a larger effective weld area and corresponding increase in weld strength.

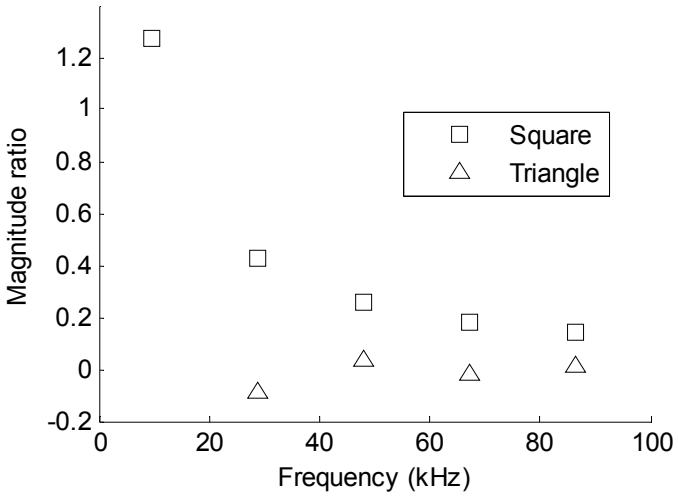

Figure 32 Frequency compositions of square and triangle waves with a 9.6 kHz fundamental frequency

A limitation with most ultrasonic welding platforms lies in their use of piezoelectric transducers, which are typically only efficient over a very narrow frequency band, thus limiting their use at any more than a small number of harmonics. Transducers based on magnetostrictive Terfenol-D typically possess a much wider frequency response, making them well suited to produce non-sinusoidal waveforms. The purpose of this paper is to investigate the effect of using square and triangle waves in comparison to more conventional sine waves.

5.2 Materials and Methods

These experiments were conducted using a custom-built machine that consists of a vibration transducer, bulk-motion transducer, and associated sensors pictured in Figure 33.

A model CU-18 Terfenol-D vibration transducer was provided by Etrema Products that includes an acoustically-tuned titanium horn that acts as the sonotrode for the welding process. All experiments were conducted at a weld frequency of 9.6 kHz, which is the location of the transverse vibration mode for the horn and provided the best weld quality. All tests were taken at the highest power setting, which offered a 4.8 μm vibration amplitude.

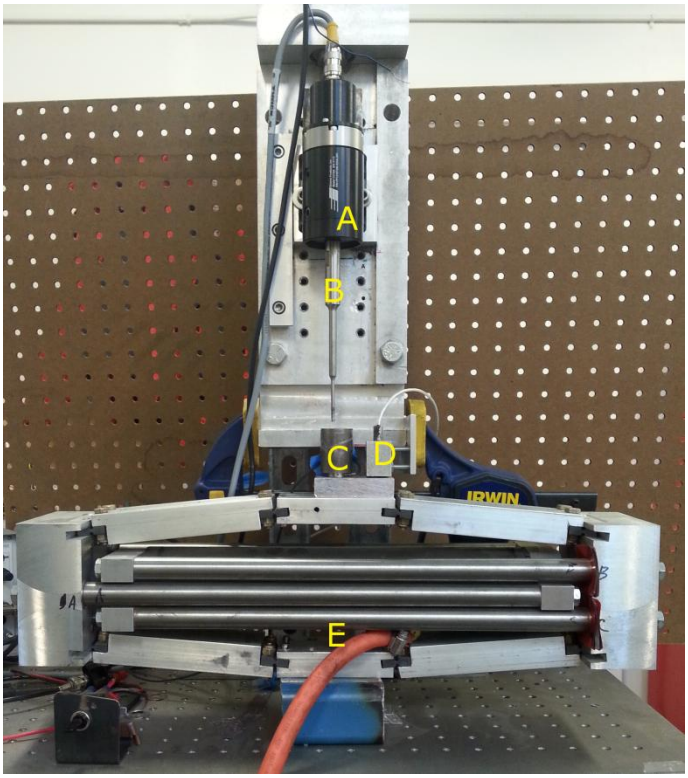

Figure 33 Experimental setup, comprised of CU-18 vibration transducer (A), titanium horn (B), lower die (C), displacement sensor (D), bulk motion transducer (E)

Clamping force and bulk motion were provided by a custom Terfenol-D transducer that includes a flextensional lever system for strain amplification, allowing for displacements of up to 1.6 mm and a blocked force of over 300 N. Full range displacement control has been demonstrated at up to 30 Hz. Its solid-state design allows for frictionless, backlash-free

movement with precision well under 1 μm, limited in this case by measurement capabilities (Witthauer, 2013).

Measurements were taken using a Kistler force transducer sandwiched between the output stage of the bulk motion transducer and the lower die and a capacitive displacement sensor that measured the position of the output stage. Data acquisition and system control were provided by an XPC Target computer system using a program written in Matlab Simulink.

Samples consisted of two sheets of 25 x 38 mm ABS placed between the lower die and horn tip. No energy director or other surface treatments were used. Due to this, the use of transverse vibration, and the frequency used, this process is best described as a high-frequency vibration spot welding process rather than an ultrasonic welding process. The first round of experiments involved determining the influence of welding parameters on the process, which aided in the selection of the best parameters for the waveform study. After welding the weld joints were tested in shear at a constant rate of 0.02 mm/s in a universal testing machine (TestResources, Inc).

0.25 and 0.5 mm ABS sheets were used in the first round of testing to capture thickness effects. ABS was chosen as it is a highly weldable amorphous thermoplastic. Three clamping force levels were chosen for the initial round of testing that consisted of the minimum and maximum force where successful welding occurred and one intermediate value. Penetration depth has been regarded as the most important parameter in vibration welding (Stokes, 1988c), so it was given the most attention with 11 values chosen for each

thickness that were bounded by the largest distance achievable and the minimum distance that resulted in a weld. Table 6 summarizes the experimental parameters for the first round of testing.

Table 6 Experimental parameters for the first round of testing

Thickness (mm)	Clamping force (N)	Penetration (μm)
0.25	47, 89, 117	15-155
0.5	94, 139, 234	25-500

For the first round of testing, the control algorithm progressed in the following steps: 1) ramp up to clamping force; 2) turn on vibration; 3) once welding penetration reaches target level, turn off vibration; and 4) maintain clamping force as weld cools. The second round of testing was conducted similarly only with one clamping force for all samples and either a sine, square, or triangle wave. All three waveforms were fed to the vibration transducer at an amplitude of 40V RMS.

5.3 Theory

Ultrasonic and vibration welding are known to occur in four distinct phases, with two methods of heating known to act sequentially depending on the phase. Much research has also been conducted on the effects of welding parameters, which give several options for a preferred control strategy.

5.3.1 Basic mechanics of vibration and ultrasonic welding

Vibration welding typically occurs in four phases (Stokes, 1988a), as can be seen in a typical displacement vs. time trace shown in Figure 34. The first phase consists of a heating

phase, where the weld zone heats up due to coulomb friction with no measurable displacement response. The second phase consists of a "transient flow" stage, where a welding zone begins to develop in a small region of plastic that has reached a temperature where viscous flow occurs. During this phase heating transitions from primarily coulomb friction to viscoelastic heating (Zhang, 2009). As the weld zone develops, penetration begins as seen in phase 2 of Figure 34. The process then develops into a steady-state flow where the heat affected zone reaches maximum film thickness, typically on the order of 0.1 mm (Suresh, 2007). The resulting flow state causes a nearly linear increase in displacement over time at a penetration rate v_o, as indicated in phase 3. This phase proceeds relatively quickly, on the order of 0.1 s (Aloiso, 1972); the high rate of deformation once phase 3 is entered is the primary reason that penetration is a more useful experimental parameter than time. If phase 3 is not terminated by turning off vibration, penetration will proceed to a level where maximum penetration is achieved, which depends heavily on the material and system used. Phase 4 is marked by the solidification and cooling of the weld zone. Penetration over this phase is relatively small.

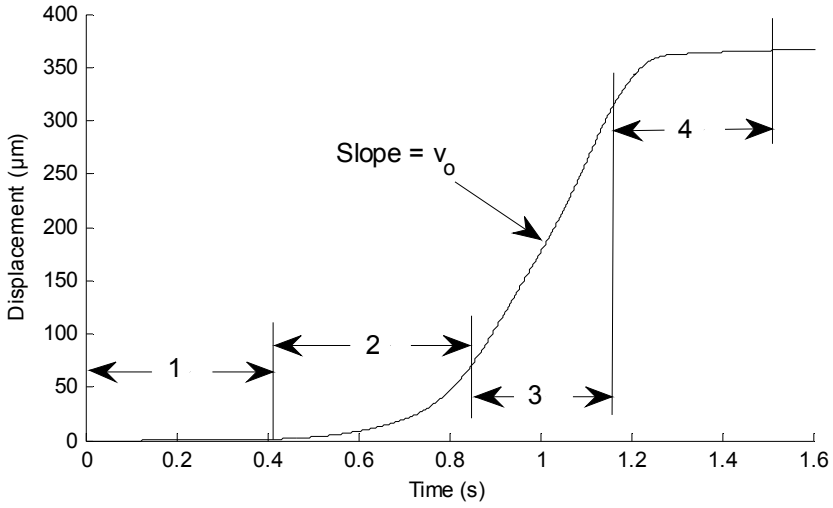

Figure 34 Phases of welding demonstrated on a welding sample of 0.5 mm thick ABS welded to 358 µm at 234 N

Surface effects are known to play an important role as well, particularly in the higher-frequency, lower-displacement scenarios found in ultrasonic welding. Significant research has been conducted on the design of energy directors, with semi-circular designs performing quite well, and simple surface texturing giving higher strength and less distortion while requiring less energy (Rani, 2009).

5.3.2 Known parameter effects

ABS is an amorphous thermoplastic that is known to weld well, although it is known to be sensitive to clamping force (Van Wijk, 1996). Material thickness has also received a good deal of attention; increasing thickness has been linked to increasing time to reach steady-state, increase in steady-state penetration, decrease in steady-state penetration rate, and an increase in steady-state molten film thickness (Stokes, 1989).

More clamping force typically results in less achievable penetration, higher penetration rates, and faster welding (Stokes, 1989). Too little pressure results in insufficient weld zone generation; too much results in fast flow of molten material, resulting in poor polymer chain alignment which causes a slight decrease in strength (Benatar, 1989b). Similar results were found with studies in advanced control where vibration amplitude was adjusted automatically in order to maintain constant force during welding (Grewell, 1996). Penetration depth has been found to be the most important experimental parameter; a critical penetration depth exists, above which full parent material strength can be achieved, and below which strength falls off quickly (Stokes, 1988d).

While it is known that full material strength can be achieved, weld zone size plays an important role in the overall strength of the joint. While penetration depth has been considered the most important factor, film thickness will also be taken into consideration in this study, as it may provide new insight into overall joint strength. Film thickness h_o differs from penetration depth in that it indicates the penetration that has occurred purely in the linear steady-state portion of phase 3 in Figure 34. Film thickness has been shown to be related to part thickness b, viscosity μ, penetration rate v_o, and clamping pressure p_o through the following relationship (Stokes, 1989):

$$\frac{h_o^3}{\mu} = \frac{4b^2 v_0}{p_o} \tag{10}$$

The primary difficulty in using this relationship is that μ changes drastically with temperature throughout the process. Another, simpler relationship based on energy analysis

based on the time t_o required to attain steady state penetration, the time spent in phase 3 is approximately given by Equation (11) (Stokes, 1989).

$$h_o = \frac{8 v_o t_o}{3} \tag{11}$$

5.4 Results and discussion

Results from the first round of testing agree with previous research and was influential to the second round waveform study. The waveform study allowed a closer look at the effect of penetration rate while offering another method of penetration rate control.

5.4.1 Strength vs. penetration for sinusoidal waveforms

Strength data for the first round of testing with sinusoidal waveforms is shown in Figure 35. Several observations can be made from this data. First note that the maximum achievable displacement approached sheet thickness, particularly with the thicker 0.5 mm samples; in these samples the top sheet is nearly completely penetrated with a ring of material around the weld indentation that holds the joint together. Failure mode for these samples was complete peel-out of the top sheet as shown in Figure 36(a). It is also worth noting that there is certainly a minimum critical penetration required for reasonable strength, as well as a peak penetration beyond which no additional strength is achieved.

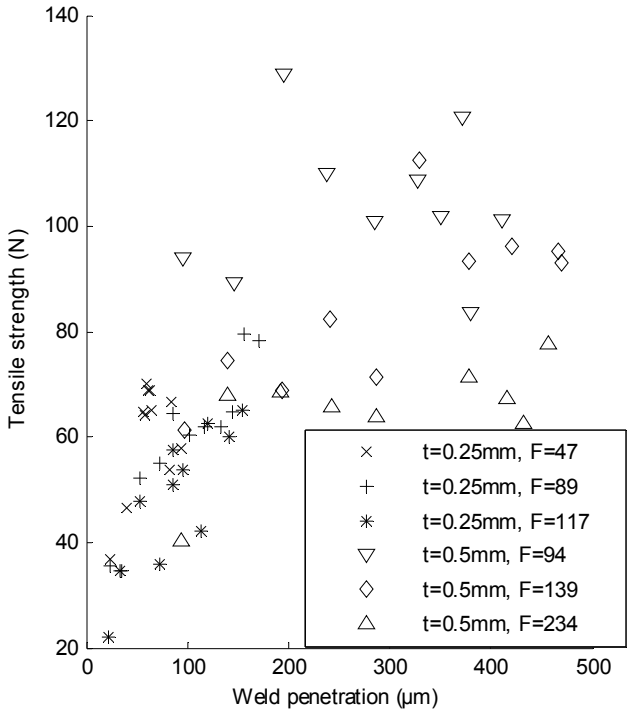

Figure 35 Strength data for first round of plastic welding testing with sinusoidal waveforms, arranged by sheet thickness and clamping force

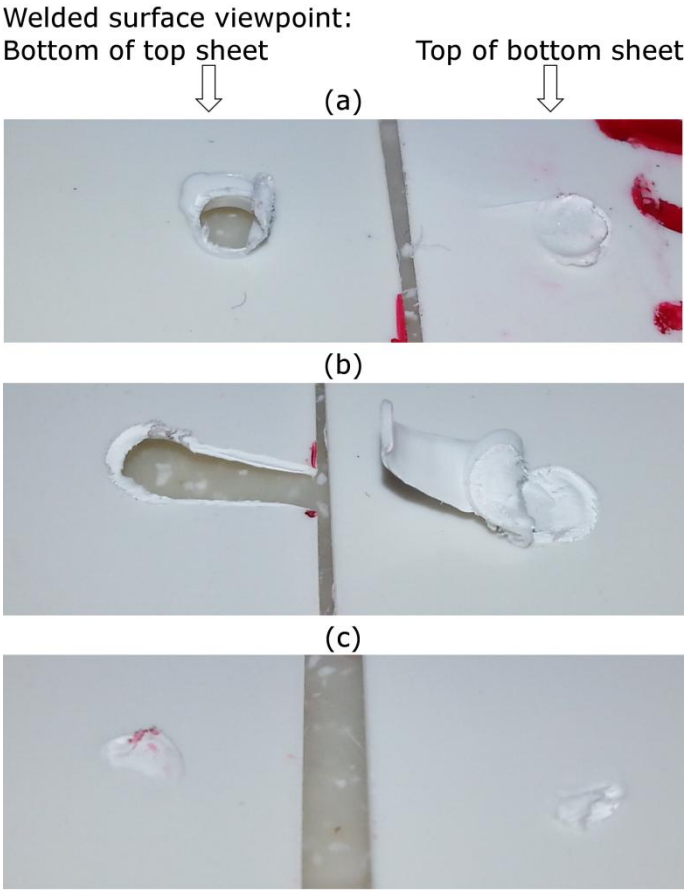

Figure 36 Plastic welding samples from first round of testing. (a) Over-penetration, resulting in complete peel-out of top layer; (b) proper penetration resulting in multiple failure modes; (c) inadequate penetration resulting in incomplete welding

The failure mode for the weaker samples was purely joint fracture, with the weakest samples showing a fracture area much smaller than the typical weld area, as shown in Figure 36(c). Conversely, the highest-strength samples experienced multiple failure modes, with an initial fracture component followed by extensive peeling of the upper or lower sheets, sometimes both as shown in Figure 36(b). This agrees well with previous work that shows that weld strengths near or equal to that of the parent material is possible. It is also apparent that higher clamping forces typically result in less strength for a given penetration.

A closer look at thickness effects can be seen in Figure 37, where penetration is expressed as a proportion of sheet thickness. From here it is apparent that proportionally less penetration could be achieved with the thinner sheet, and the highest strength occurred in both sets around 60% of sheet thickness. For the thinner sheet this was also the highest penetration, which was achieved with intermediate clamping load. It is also worth noting that the intermediate clamping force for the thin sheet was very close to the smallest clamping force for the thicker sheet, which indicates that the optimum clamping force does not appear to depend significantly on sheet thickness. These observations indicate that for this material and experimental setup, waveform testing should be conducted with a clamp load around 90 N across a series of penetration depths. Minimum penetration depths of 50 and 75 μm were chosen for the 0.25 and 0.5 mm sheets, respectively.

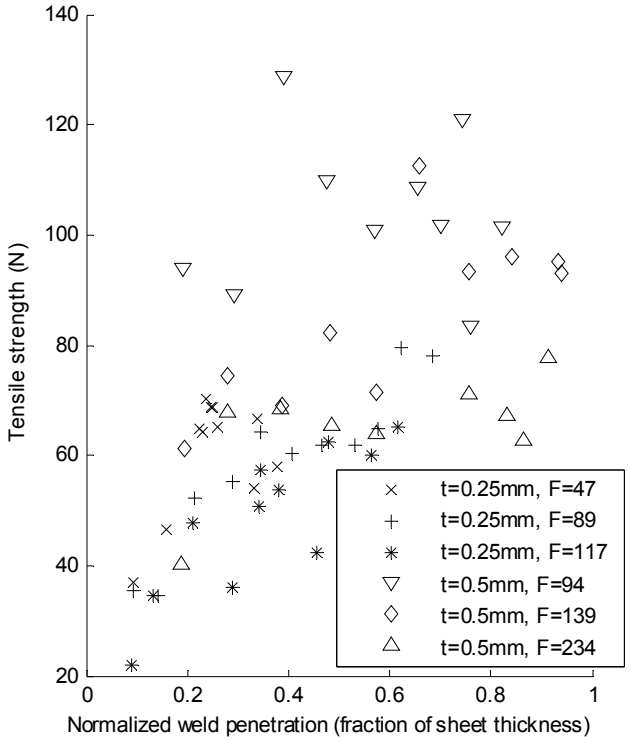

Figure 37 Strength as a function of normalized penetration, arranged by sheet thickness and clamping force

Film thicknesses were calculated using Equation (11) using the penetration rate v_o and phase 3 times from test data, which were found using an algorithm in Matlab developed to fit a line to the displacement-time trace at the mid-point of phase 3 and calculate the duration of phase 3 based on a deviation of more than 0.05 s from this line. Because the calculation is based on a deviation from linearity, it captures the amount of steady-state penetration from phase 3 while cutting out transient penetration seen in phases 2 and 4. The results of this analysis are shown in Figure 38. Not surprisingly, a nearly direct correlation between penetration depth and film thickness was found. One interesting trend from this data appears

when looking at the upper and lower fringes of the distribution; lower clamping forces resulted in slightly lower film thicknesses for a given penetration, and vice versa. Given that higher clamping loads resulted in both thicker films and less strength, the hypothesis that higher clamping loads results in unfavorable polymer chain alignment gains more support, as well as the claims that higher clamping force welds develop steady state flow more quickly.

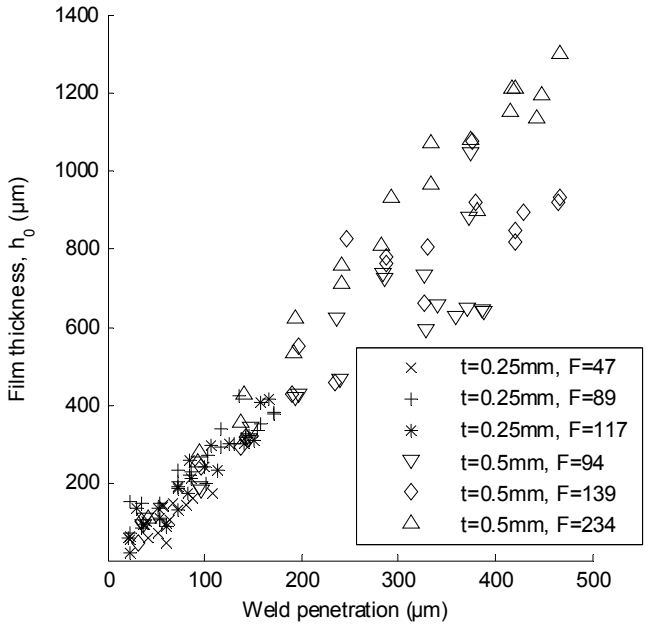

Figure 38 Film thickness calculated from displacement trace data as a function of penetration depth

This hypothesis gains further support when directly comparing joint strength with penetration rate in Figure 39, where high forces clearly result in the highest penetration rate and a significant reduction from peak strength. It appears that for both thicknesses, peak strength occurs at a penetration rate just below 500 µm/s with around 90 N of clamping force.

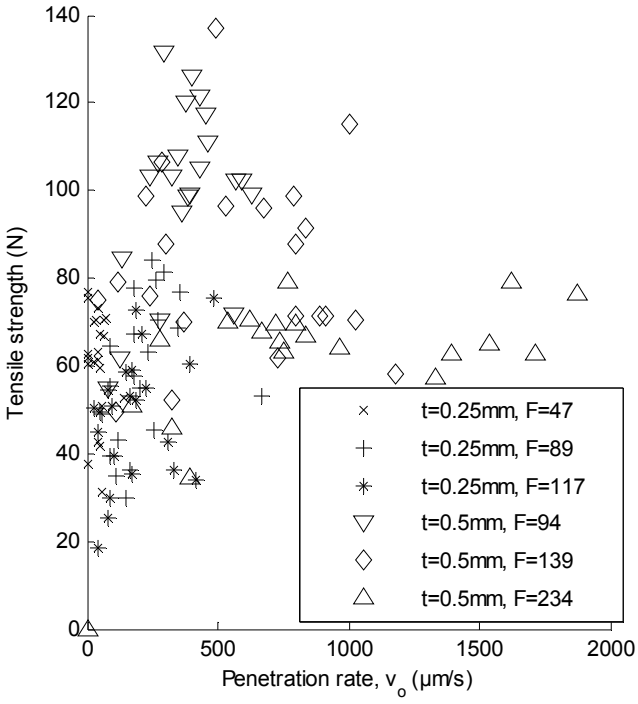

Figure 39 Impact of penetration rate on strength, first round of testing

5.4.2 Strength vs. penetration for square and triangle waveforms

Figure 40 summarizes the effects of penetration and waveform on weld strength found in the second round of testing. From the standpoint of strength, in the thicker samples the square and sine waves performed quite similarly, with the triangle waves performing slightly better overall, again with peak strength occurring around 60% of sheet thickness. In the thinner sheet however, the triangle wave specimens were not capable of adequate penetration or strength, with the square wave slightly outperforming the sine wave, again with peak strength occurring in the vicinity of 60% of sheet thickness.

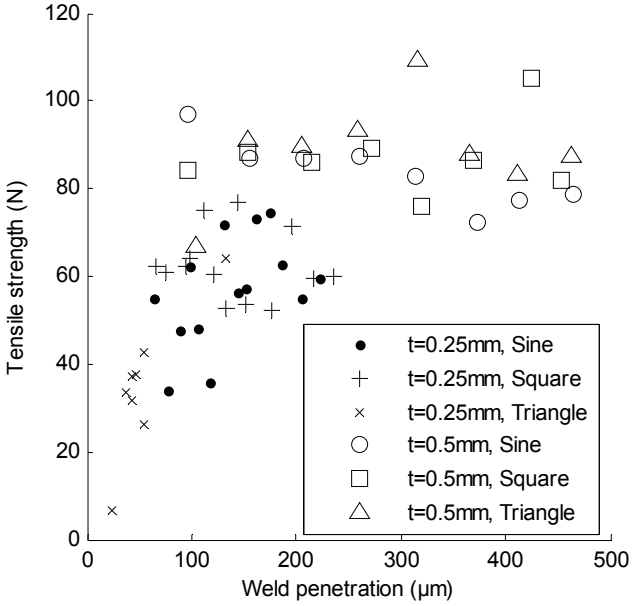

Figure 40 Effect of waveform and penetration on weld strength, second round of testing

A closer look at penetration rates helps differentiate the effects of the different waveforms. From Figure 41 it can be seen that in the thicker samples when using square or sine waves, peak strength still occurred around 500 µm/s, dropping off with higher penetration rates. In the thicker samples where the triangle wave fared better, peak strength was observed with a much smaller 240 µm/s penetration rate, while consistently showing higher strength and lower penetration rates. In the thinner sheets, however, the slower penetration rates exhibited by the triangle waves were not capable of providing ample penetration for strong welds. In all cases, square waves provided slightly higher penetration rates than sine waves.

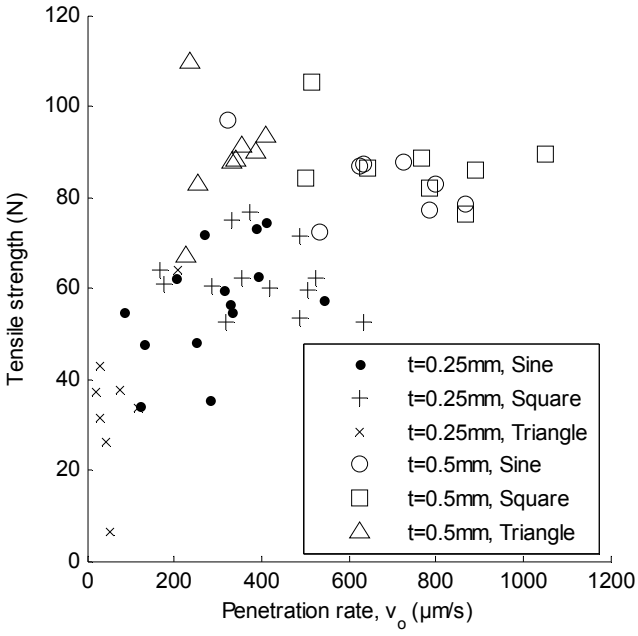

Figure 41 Effect of waveform and penetration rate on weld strength, second round of testing

Figure 42 combines the ideas from Figure 40 and Figure 41 to elucidate the combined effects of penetration and penetration rate between the different waveforms. Again in all samples square waves showed higher penetration rates, but only slightly higher penetration than sine waves. At lower levels of penetration the correlation appeared more direct than at higher levels. Again with the thinner sheet triangle waves were on the bottom of the scale, but in the thicker sheet showed a strong divergence of the correlation between penetration and penetration rate, where the depth of penetration was capable of increasing drastically with almost no increase in penetration rate.

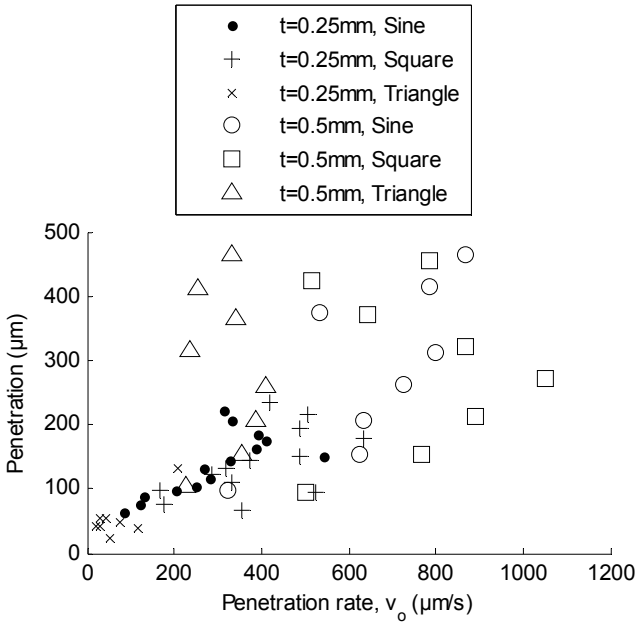

Figure 42 Effect of waveform on penetration and penetration rate, second round of testing

5.5 Conclusions

For this application of high-frequency vibration welding using thin sheets of ABS plastic without an energy director, low to moderate clamping loads and moderate to high penetration offered the best strength, although strength gains diminished after penetrations of 60% sheet thickness. Optimal clamping loads were independent of sheet thickness. Thinner sheets were capable of less penetration and strength than thicker sheets. Film thickness had a nearly direct correlation to weld penetration, with a minor reduction in film thickness per penetration with less clamping load, although the corresponding lack of strength under higher clamping load lends support to the idea that higher clamping loads result in poor polymer chain alignment.

Different waveforms impacted both penetration and penetration rate, with their own associated thickness effects. Square waves displayed the highest penetration rates, which were beneficial in the thinner samples where the large penetration depths needed for high strength were difficult to achieve. In thicker sheets where optimal penetration was easier to achieve, the balance turned to favor triangle waves, as their lower penetration rates provided increased strength that was likely due to more favorable polymer chain alignment.

Therefore it is concluded that:

1. In general, square waves typically result in slightly higher penetration rates than sine waves, and significantly higher penetration rates than triangle waves
2. This penetration rate effect due to waveform is similar to the penetration rate effect caused by clamping forces, in that lower penetration rates result in higher strengths
3. The penetration rate effect is still dominated overall by the penetration depth effect, and penetration rates below a certain threshold are not capable of providing large penetration depths

CHAPTER 6. SUMMARY AND SCIENTIFIC CONTRIBUTIONS

6.1 Summary

Overall this body of research has demonstrated the functionality of a desktop microforming system driven by Terfenol-D that takes advantage of the benefits offered by ultrasonic forming. A Terfenol-D transducer for bulk motion was designed, fabricated, tested, and modeled, and its electro-mechanical, thermal, and frequency response was characterized. This transducer was then coupled to a lever system unique in its use of bolt-on flexure joints that proved devoid of friction or backlash. Overall this system is capable of sub-micron resolution, currently limited by measurement noise and not the system itself. A system model was created that could prove useful in the design of flexure joints by providing a simulation of the tradeoffs between joint stiffness and resistance to motion. This model can also be used for more intensive simulations on energy consumption or other items of interest in order to compare feasibility and performance to other types of systems. More importantly, with these characteristics defined and modeled, this design may well serve as a basis for various other applications. Its solid state, friction and backlash-free design offer several unique advantages over other types of drive or positioning systems.

Ultrasonic-assisted punching was found to offer several improvements over conventional punching, including reduced punching force, a reduction in adiabatic strain rate effects, and an increase in the overall proportion of burnished to fractured area.

The plastic welding process described here expanded upon several trends observed in both ultrasonic welding and vibration welding, and took a look at the effects of square and triangle vibration waveforms on the process. This comparison took a closer look at penetration rates and film thickness than previous studies, and made new connections between strength, penetration rates, and achievable penetration depths, as well as a new method of influencing penetration rates.

6.1.1 Design and characterization of a high-power, low-frequency Terfenol-D transducer for use in microforming

The Terfenol-D transducer outlined in Chapter 2 performed as expected, with a blocked force of 3.8 kN and 212 μm of travel. The magnetic response was examined and subsequently improved. While the magnetic system did not receive a great deal of attention, it is important as the magnetic reactance affects the overall efficiency of the system. An efficient flux return path results in greater magnetic response per voltage input, thereby increasing system output per voltage input. A simple linear model was developed to predict the maximum force output available from the system as a function of displacement at magnetic saturation, which matched experimental output of the system within 10%. The major findings from this study were that:

(1) Mechanical preload has a large effect on the response of Terfenol-D. The majority of research on Terfenol-D has been in cyclic applications where additional preload reduces hysteresis, with recommended preload in the vicinity of 20 MPa (Dapino, 2004). This application showed maximum output with a much lower preload of 3.4 MPa.

Consequently, hysteresis significantly reduced system output as frequencies increased over 5 Hz, with overall displacement nearly halved by 20 Hz. Additionally, the requirement for a low spring rate in the preload system was made evident in thermal testing, where 44 μm of thermal drift resulted in a 10% reduction in output displacement.

(2) With a maximum power consumption of 2.5 kW, thermal considerations are not to be underestimated. Thermal drift occurred at 2 μm/ºC, or 1% per degree-Celsius. Combining thermal drift with the 10% loss in range that accompanied just 20ºC of heating limits the amount of compensation that can be obtained through control strategies, which highlights the importance of the transducer's cooling system. With basic compressed air cooling, maximum duty cycle for 1ºC temperature stability was around 10% for a sinusoidal input. This likely would not be considered acceptable for an industry application, and therefore a more aggressive cooling strategy, perhaps the use of a water-cooled coil, would be necessary.

(3) From a mechanical design aspect, an important factor is designing the system for purely axial loading on the Terfenol-D rod. Bending loads are not only undesirable from a structural standpoint, but also causes angular deflection which adds binding and friction to the system. Manufacturing tolerances are important, and use of a common reference eliminates tolerance stackup. All of these accommodations combined resulted in a lack of measurable friction with a minimum resolution of <100 nm based on full system analysis and an effective lever ratio of 10.

6.1.2 Design and characterization of a displacement amplification system for use in microforming

The unconventional bolt-on flexure joint design performed on par with expensive monolithic systems. A model of the overall system showed an 11% error in prediction of maximum force, but only a 2% error in free displacement. The lever system added no perceivable backlash or friction to the system, giving an overall minimum system displacement resolution of <1 μm, limited by measurement noise. Frequency response was not considered closely in this work, but designing for higher operating frequencies could offer improvements with regards to power consumption due to reduced cycle times. This research led to the following conclusions:

(1) A multi-piece flextensional lever system could reduce cost, especially on a system as large as this, but manufacturing tolerance stackup can cause difficulties in assembly and adversely affect the system's motion. This can be overcome to an extent by measuring and matching tolerances between components. Besides the cost, another benefit to the multi-piece lever system design is the ease of replacing joints, which allows for both experimentation with joint design and ease of repair if a joint is damaged.

(2) The portion of the system model consisting of the lever system is likely much more accurate than these results suggest. The nonlinearity in the overall system model is almost exclusively due to the nonlinearity error in the transducer model being propagated into the full system model, while the components of the lever system itself are nearly linearly elastic. Given the complex geometry of typical flexure joints, FEM and empirical

relationships have become the primary methods for flexure joint design (Yong, 2008). This model represents a good system tool that could interface nicely with FEM for a systems design approach or a numerical optimization.

(3) Several mechanical design considerations were important in the development of the multi-piece flextensional lever system. Elimination of friction posed no significant challenge as there are no moving components; this is no different from a typical monolithic flextensional system, assuming the bolted joints fit tightly. Backlash is eliminated for the multi-component design by ensuring that all components have interference fits. To achieve this constraint without requiring excessively tight machine tolerances, press-fit pins were used whenever possible to attach components. In locations where bolted joints were in shear, precision-ground close-fit AN-spec shoulder bolts were used.

6.1.3 Experiments and analysis in ultrasonic-assisted punching in aluminum

Several conclusions can be drawn from the studies on ultrasonic-assisted punching:

(1) The experiments with the higher 100 μm/s punching speed without vibration displayed significantly higher punching force than the 50 μm/s samples without vibration. The shape of the force profile was also qualitatively similar to those encountered at increased punching rates in the same material (Blazynski, 1987), indicating an adiabatic strain rate hardening effect was present. Small to moderate vibration amplitude yielded similar results to lower speed testing, indicating a negation of adiabatic strain rate effects, while high vibration amplitude at the higher speed resulted in the greatest impact on punching force, with a reduction of 30%.

(2) At the lower 50 µm/s punching speed only moderate reductions in punching force were observed for all vibration amplitudes. This reduced level of softening is hypothesized to be caused by acoustoplastic hardening, as the sample is exposed to vibration for double the length of time as the higher punching speed results. This agrees with previous research on acoustoplastic hardening (Yao, 2012a).

(3) While the lower speed samples showed moderate reductions in punching force in response to vibration, they showed a noticeable increase in the proportion of burnished to fractured area present, indicating increased ductility. This effect was not nearly as prominent in the higher speed punching results.

(4) Adiabatic strain rate hardening is marked by a localized reduction in temperature that results in reduced dislocation mobility due to reduced thermal vibrations. Ultrasonic softening is marked by an increase in dislocation mobility caused by direct application of vibration. Both processes function through dislocation mobility, so it makes sense that ultrasonic softening can counteract adiabatic strain rate hardening. The functional equivalence of ultrasonic softening to thermal effects also supports the idea of modelling ultrasonic softening similarly to a thermal process as performed in previous research (Yao, 2012a).

6.1.4 The effect of waveform on polymer vibration welding in ABS plastic

Several new observations were made while investigating the effect of waveform on vibration welding, including a more in-depth look at previously observed phenomena.

(1) In general, square waves typically result in slightly higher penetration rates than sine waves, and significantly higher penetration rates than triangle waves. This makes sense intuitively, as the frequency composition of a square wave is composed of a higher magnitude fundamental frequency accompanied by a series of harmonics that quickly drop in magnitude, while a triangle wave is composed of a series of harmonics of alternating sign that maintain significant magnitude over a much wider frequency range.

(2) This penetration rate effect due to waveform is similar to the penetration rate effect caused by clamping forces, in that lower penetration rates result in higher strengths.

(3) The penetration rate effect is still dominated overall by the penetration depth effect, and penetration rates below a certain threshold are not capable of providing large penetration depths.

6.2 Scientific contributions

The major scientific contributions of this dissertation may be summarized as follows:

1. During the process of characterizing the Terfenol-D transducer it was discovered that published ranges for several parameters, particularly pre-stress, were not adequate for good performance in a low-frequency application. Most previous research on applications of Terfenol-D has focused on systems that operate in the acoustic to ultrasonic frequency range, with much less research conducted on low-frequency systems; there was previously little reason to believe that a low-frequency transducer would behave completely differently.

2. The majority of previous research on modeling the magnetostrictive response of Terfenol-D has focused on accurately representing nonlinear effects. While capturing these

effects is useful, it can make prediction of a transducer's overall response cumbersome. When designing a transducer to operate in the DC to low-frequency range, a snapshot of the maximum elastic response has been found to be both convenient and surprisingly accurate at predicting the overall material response at constant DC field strength.

3. Flextensional lever systems have seen considerable research as well, although most are built using models based on either FEM or complex stiffness matrices. The flextensional lever system model developed in this research was found to be not only very accurate at predicting overall system response, but also simple and flexible enough to allow exploration of the competing effects of different joint parameters.

4. This is the first known research on ultrasonic softening applied to a process that depends on fracture, as well as the first investigation of ultrasonic softening on strain rate effects. Adiabatic strain rate hardening and ultrasonic softening were found to be competing effects both based on dislocation mobility, and as such ultrasonic softening was discovered to overcome adiabatic strain rate effects. At lower punching speeds where adiabatic strain rate effects were not observed, increased vibration resulted in larger proportions of burnished to fractured areas, indicating increased overall ductility in the presence of ultrasonic softening.

5. The waveform study in ABS plastic welding reinforced the importance of penetration depth in plastic welding and brought new light to old ideas on penetration rate effects. The ability to manipulate penetration rates with waveform rather than clamping force resulted in a significant increase the strength of plastic welds, but the most interesting feature is the ability to achieve much higher penetration depths at low penetration rates when

using triangle waves. The increased penetration rate observed when using square waves also displayed another avenue of achieving greater penetration depth in harder to weld thin-cross-section materials; this effect could also potentially be used to improve the welding of difficult to weld semi-crystalline polymers.

BIBLIOGRAPHY

Dapino, M. (2004) On magnetostrictive materials and their use in adaptive structures, Structural Engineering and Mechanics, 17, 3-4, pp. 303-329.

Sapozhnikov, K. V. (1997) Acoustoplastic effect and internal friction of aluminum single crystals in various deformation stages, Physics of the Solid State, 39, 10, pp. 1601-1606.

Yong, Y. K. (2008) Review of circular flexure hinge design equations and derivation of empirical formulations, Precision Engineering, 32, pp. 63-70.

Cao, J. (2004) Microforming: Experimental Investigation of the Extrusion Process for Micropins and its Numerical Simulation Using RKEM, Transactions of ASME, 126, pp. 642-652.

Culp, D. R. (1973) Metal deformation with ultrasound, Ultrasonics Symposium, pp. 195-198.

Dawson, G. R. (1970) Application of High-Frequency and Low-Frequency Oscillations to the Plastic Deformation of Metals: Part 2--A Complete Appraisal of the Development and Potential, Metal Forming, 37, 9, pp. 254-261.

Devine, J. (1981) Ultrasonic cold forming of aircraft sheet metals, U.S. Army Aviation Research and Development Command,

Engel, U. (2002) Microforming--from basic research to its realization, Journal of Materials Processing Technology, 125-126, pp. 35-44.

Huang, H. (2009) Influence of superimposed ultrasound on deformability of Cu., Journal of Applied Physics, 106, 113514, pp. 1-6.

Izumi, O. (1966) Effects of Superimposed Ultrasonic Vibration on Compressive Deformation of Metals, Trans. Jpn. Inst. Met., 7, 3, pp. 162-167.

Jimma, T. (1998) An application of ultrasonic vibration to the deep drawing process, Journal of Materials Processing Technology, 80-81, pp. 406-412.

Langenecker, B. (1966) Effects of Ultrasound on Deformation Characteristics of Metals, IEEE Transactions on Sonics and Ultrasonics, SU-13, 1, pp. 1-8.

Langenecker, B. (1981) Ultrasonic drawing of fine wires, Wire Journal, Sept., pp. 246-248.

Lucas, M. (1996) Vibration sensitivity in the design of ultrasonic forming dies, Ultrasonics, 34, pp. 35-41.

Ngaile, G. (2008) Influence of ultrasonic vibration on microforming, Transactions of the North American Manufacturing Research Institution of SME, 36, pp. 137-144.

Presz, W. (2007) Flexible Manufacturing System for Vibration Assisted Microforming, 10th ESAFORM Conference on Material Forming, pp. 677-682.

Rosochowski, A. (2007) Micro-extrusion of ultra-fine grained aluminium, International Journal of Advanced Manuracturing Technology, 33, pp. 137-146.

Sapozhnikov, K. V. (1997) Acoustoplastic effect and internal friction of aluminum single crystals in various deformation stages, Physics of the Solid State, 39, 10, pp. 1601-1606.

Schinke, B. (1987) Dynamic Tensile Tests with Superimposed Ultrasonic Oscillations for Stainless Steel Type 321 at Room Temperature, Nuclear Engineering Design, 100, 3, pp. 281-296.

Siegert, K. (2001) Influencing the Friction in the Metal Forming Processes by Superimposing Ultrasonic Waves, CIRP Ann-Manuf. Technol, 50, 1, pp. 195-200.

Storck, H. (2002) The effect of Friction Reduction in Presence of Ultrasonic Vibrations and its Relevance to Travelling Wave Ultrasonic Motors, Ultrasonics, 40, 1-8, pp. 379-383.

Winsper, C. E. (1970) An Introduction to the Mechanics of Oscillatory Metalworking, Metallic Materials, 4, 4, pp. 158-162.

Yao, Z. (2012) Acoustic softening and residual hardening in aluminum: modeling and experiments, International Journal of Plasticity, 39, pp. 75-87.

Aloiso, C. J. (1972) A simplified thermoviscoelastic analysis of the ultrasonic bonding, paper presented at Annual Technical Conference / Society of Plastic Engineers, 1972.

Bacher, J.-P. (2002) Flexures for high precision robots, *Industrial Robot: An International Journal*, **29**, 4, pp. 349-353.

Baker, G. S. (1967) Dislocation Mobility and Motion under Combined Stresses, *Journal of Applied Physics*, **38**, 4, pp. 1586-1591.

Bartlett, P. A. (2001) High-power, low frequency magnetostrictive actuation for anti-vibration applications, *Sensors and Actuators A*, **91**, pp. 133-136.

Becze, C. E. (2001) High strain rate shear evaluation and characterization of AISI D2 tool steel in its hardened state, *Machining Science and Technology*, **5**, 1, pp. 131-149.

Benatar, A. (1989a) Ultrasonic Welding of Thermoplastics in the Far-Field, *Polymer Engineering and Science*, **29**, 23, pp. 1699-1704.

Benatar, A. (1989b) Ultrasonic Welding of Thermoplastics in the Near-Field, *Polymer Engineering and Science*, **29**, 23, pp. 1689-1698.

Blaha, F. and Langenecker, B. (1955) Dehnung von Zink-Kristallen unter Ultraschalleinwirkung, *Naturwissenschaften*, **42**, 20, pp. 556-556.

Blazynski, T. Z. (1987) *Materials at High Strain Rates*, Springer,

Claeyssen, F. (1997) Actuators, transducers, and motors based on giant magnetostrictive materials, *Journal of Alloys and Compounds*, **258**, pp. 61-73.

Culp, D. R. (1973) Metal deformation with ultrasound, *Ultrasonics Symposium*, pp. 195-198.

Dapino, M. (2004) On magnetostrictive materials and their use in adaptive structures, *Structural Engineering and Mechanics*, **17**, 3-4, pp. 303-329.

Daud, Y. (2007) Modelling the effects of superimposed ultrasonic vibrations on tension and compression tests of aluminium, *Journal of Materials Processing Technology*, **186**, pp. 179-190.

Devine, J. (1981) *Ultrasonic cold forming of aircraft sheet metals*, U.S. Army Aviation Research and Development Command,

Engel, U. (2002) Microforming--from basic research to its realization, *Journal of Materials Processing Technology*, **125-126**, pp. 35-44.

Grewell, D. A. (1996) Amplitude and force profiling: Studies in ultrasonic welding of thermoplastics, *Annual Technical Conference - ANTEC*, Society of Plastics Engineers, pp. 1188-1192.

Hayashi, M. (2003) Simulation of ultrasonic-vibration drawing using the finite element method (FEM), *Journal of Materials Processing Technology*, **140**, pp. 30-35.

Hayden, H. W. M., William G; Wulff, John (1965) *The structure and properties of materials, Vol. 3*, Wiley, New York, London.

Jimma, T. (1998) An application of ultrasonic vibration to the deep drawing process, *Journal of Materials Processing Technology*, **80-81**, pp. 406-412.

Kalpakjian, S. (2003) *Manufacturing Processes for Engineering Materials*, Pearson Education,

Kang, B. H. (2005) Analysis and Design of Parallel Mechanisms with Flexure Joints, *IEEE Transactions on Robotics*, **21**, 6, pp. 1179-1185.

Langenecker, B. (1966) Effects of Ultrasound on Deformation Characteristics of Metals, *IEEE Transactions on Sonics and Ultrasonics*, **SU-13**, 1, pp. 1-8.

Langenecker, B. (1973) Basic and applied research on metal deformation in macrosonic fields at PVL-Austria, *Ultrasonics International*, Imperial College, London, pp. 34-37.

Langenecker, B. (1981) Ultrasonic drawing of fine wires, *Wire Journal*, **Sept.**, pp. 246-248.

Li, J. H. (2002) Research of the plastic status parameter and instantaneous clearance of a punching without burr, *Journal of Materials Processing Technology*, **129**, pp. 305-309.

Ling, S.-F. (2006) Input electrical impedance as signature for nondestructive evaluation of weld quality during ultrasonic welding of plastics, *NDT&E International*, **39**, pp. 13-18.

Lo, S.-P. (2010) Relationship between the Punch-Die Clearance and Shearing Quality of Progressive Shearing Die, *Materials and Manufacturing Processes*, **25**, 8, pp. 786-792.

Lucas, M. (1996) Vibration sensitivity in the design of ultrasonic forming dies, *Ultrasonics*, **34**, pp. 35-41.

Malygin, G. A. (2000) Acoustoplastic Effect and the Stress Superimposition Mechanism, *Physics of the Solid State*, **42**, 1, pp. 72-78.

Meyer, R. J., Jr. (2001) Displacement amplification of electroactive materials using the cymbal flextensional transducer, *Sensors and Actuators A*, **87**, pp. 157-162.

Moffett, M. B. (1991) Characterization of Terfenol-D for magnetostrictive transducers, *J. Acoust. Soc. Am*, **89**, 3, pp. 1448-1455.

Moffett, M. B. (1993) Demonstration of the power-handling capability of Terfenol-D, *J. Acoust. Soc. Am*, **93**, 3, pp. 1653-1654.

Moffett, M. B. (1995) High-Power Terfenol-D Flextensional Transducer, *NUWC-NPT Tech Doc*, Pennsylvania State University, University Park, Pennsylvania,

MoriSeiki (2012) *Micro-Machining*, viewed 5 December 2013, http://www.dmgmoriseikiusa.com/micro-machining

Ngaile, G. (2008) Influence of ultrasonic vibration on microforming, *Transactions of the North American Manufacturing Research Institution of SME*, **36**, pp. 137-144.

Nonhof, C. J. (1996) Estimates for Process Conditions During the Ultrasonic Welding of Thermoplastics, *Polymer Engineering and Science*, **36**, 9, pp. 1177-1183.

Olabi, A. G. (2008) Design and application of magnetostrictive materials, *Materials and Design*, **29**, pp. 469-483.

Products, E. *Active Machining Systems (AMS)*, viewed 5 December 2013, http://www.etrema-usa.com/products/ams/

Rani, M. R. (2009) Study of different joints for ultrasonic welding of semicrystalline polymers, *Experimental Techniques*, **33**, 4, pp. 36-42.

Rolt, K. D. (1990) History of the flextensional electroacoustic transducer, *J. Acoust. Soc. Am*, **87**, 3, pp. 1340-1349.

Sapozhnikov, K. V. (1997) Acoustoplastic effect and internal friction of aluminum single crystals in various deformation stages, *Physics of the Solid State*, **39**, 10, pp. 1601-1606.

Siegert, K. (1996) Wire drawing with ultrasonically oscillating dies, *Journal of Materials Processing Technology*, **60**, pp. 657-660.

Siegert, K. (2001) Superimposing Ultrasonic Waves on the Dies in Tube and Wire Drawing, *Journal of Engineering Materials and Technology*, **123**, pp. 517-523.

Stevenson, R. (1999) A reassessment of the extrapolation technique for determining parasitic cutting loads under orthogonal cutting in strain-rate hardening materials, *Machining Science and Technology*, **3**, 1, pp. 1-8.

Stokes, V. K. (1988a) Vibration Welding of Thermoplastics Part I: Phenomenology of the Welding Process, *Polymer Engineering and Science*, **28**, 11, pp. 718-727.

Stokes, V. K. (1988b) Vibration Welding of Thermoplastics Part II: Analysis of the Welding Process, *Polymer Engineering and Science*, **29**, 11, pp. 728-739.

Stokes, V. K. (1988c) Vibration Welding of Thermoplastics Part III: Strength of Polycarbonate Butt Welds, *Polymer Engineering and Science*, **28**, 15, pp. 989-997.

Stokes, V. K. (1988d) Vibration Welding of Thermoplastics Part IV: Strengths of Poly(Butylene Terephthalate), Polyetherimide, and Modified Polyphenylene Oxide Butt Welds, *Polymer Engineering and Science*, **28**, 15, pp. 998-1008.

Stokes, V. K. (1989) Thickness Effects in the Vibration Welding of Polycarbonate, *Polymer Engineering and Science*, **29**, 23, pp. 1683-1688.

Suresh, K. S. (2007) Modeling of temperature distribution in ultrasonic welding of thermoplastics for various joint designs, *Journal of Materials Processing Technology*, **186**, pp. 138-146.

Truckenmüller, R. (2006) An ultrasonic welding based process for building up a new class of inert fluidic microsensors and -actuators from polymers, *Sensors and Actuators A*, **132**, pp. 385-392.

Tsujino, J. (2004) Welding characteristics of 27, 40, and 67 kHz ultrasonic plastic welding systems using fundamental- and higher-resonance frequencies, *Ultrasonics*, **42**, pp. 131-137.

Van Wijk, H. (1996) Process Optimization of Ultrasonic Welding, *Polymer Engineering and Science*, **36**, 9, pp. 1165-1176.

Witthauer, A. (2013) Design and characterization of a flextensional stage based on Terfenol-D actuator, *International Journal of Precision Engineering and Manufacturing*, **In press**,

Yao, Z. (2012a) Acoustic softening and residual hardening in aluminum: modeling and experiments, *International Journal of Plasticity*, **39**, pp. 75-87.

Yao, Z. (2012b) Effects of superimposed high-frequency vibration on deformation of aluminum in micro/meso-scale upsetting, *Journal of Materials Processing Technology*, **212**, pp. 640-646.

Yong, Y. K. (2008) Review of circular flexure hinge design equations and derivation of empirical formulations, *Precision Engineering*, **32**, pp. 63-70.

Zhang, Z. (2009) Study on Heating Process of Ultrasonic Welding for Thermoplastics, *Journal of Thermoplastic Composite Materials*, **23**, pp. 647-664.